Investigation of multi-ion heat and neoclassical transport using new edge main ion measurements at ASDEX Upgrade

To cite this article: P. Cano-Megias *et al* 2025 *Nucl. Fusion* **65** 096027

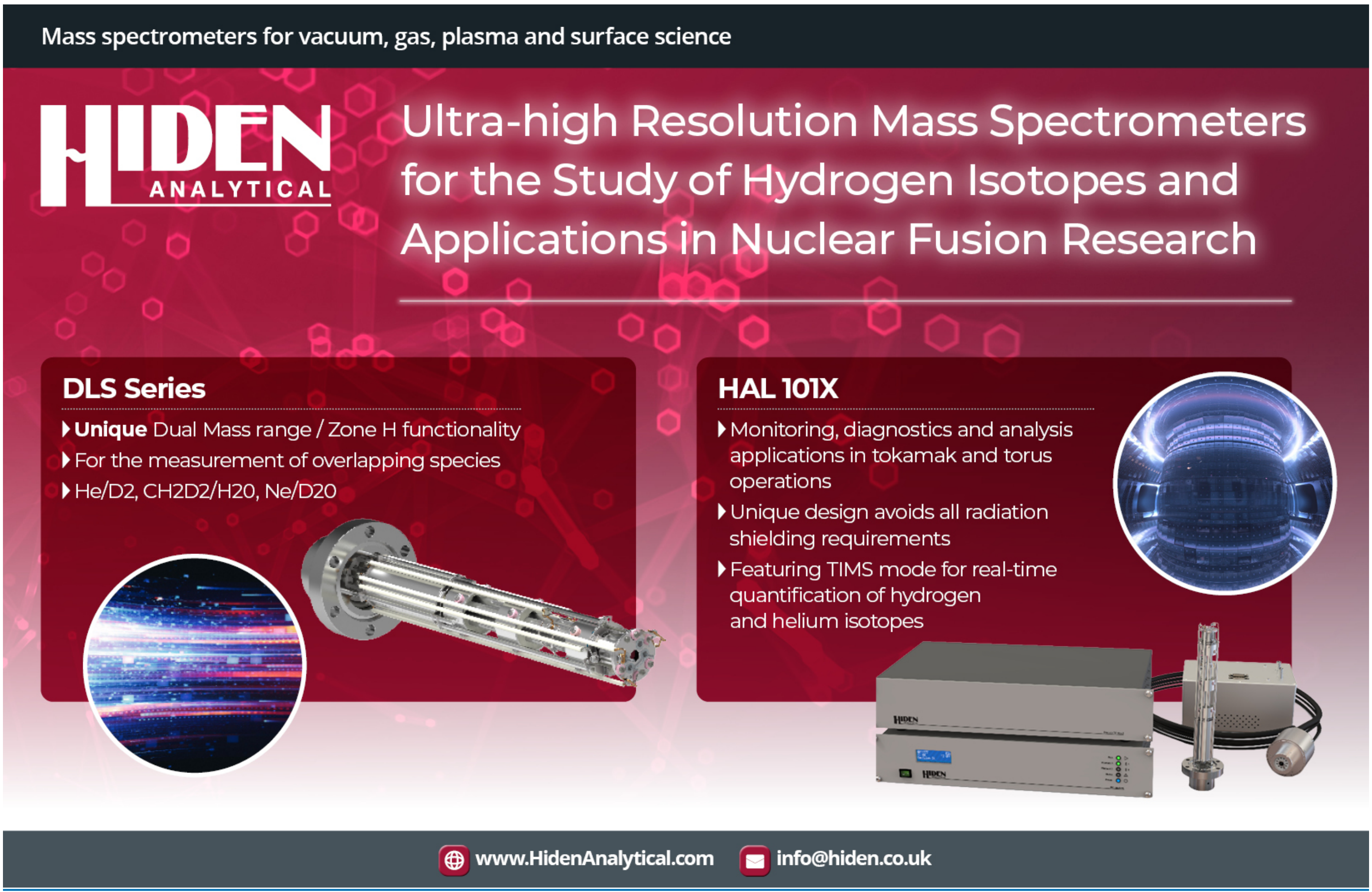

OPEN ACCESS
IOP Publishing | International Atomic Energy Agency
Nuclear Fusion
Nucl. Fusion **65** (2025) 096027 (22pp)
https://doi.org/10.1088/1741-4326/adf3cb

Investigation of multi-ion heat and neoclassical transport using new edge main ion measurements at ASDEX Upgrade

P. Cano-Megias[1,2,*], E. Viezzer[2], R.M. McDermott[1], C. Angioni[1], E. Fable[1], A. Jansen van Vuuren[3], M. Cavedon[4], D.J. Cruz-Zabala[2], R. Dux[1], P. Manas[5], J. P.-Gonzalez[2], R. Takacs[1], C.F.B. Zimmermann[1,6], R. Chacartegui[2], the ASDEX Upgrade Team[a] and the EUROfusion Tokamak Exploitation Team[b]

[1] Max Planck Institute for Plasma Physics, Boltzmannstr. 2, 85748 Garching, Germany
[2] University of Seville, Seville, Spain
[3] École Polytechnique Fédérale de Lausanne, Lausanne, Switzerland
[4] Dipartimento di Fisica G. Occhialini“, Università di Milano-Bicocca, Milano, Italy
[5] CEA, IRFM, F-13108 Saint-Paul-lez-Durance, France
[6] Department of Applied Physics and Applied Mathematics, Columbia University, New York, NY 10027, United States of America

E-mail: pcano1@us.es

Received 2 April 2025, revised 17 July 2025
Accepted for publication 23 July 2025
Published 21 August 2025

Abstract

This study provides new insights into multi-ion heat transport and the validation of neoclassical theory at the edge of H-mode plasmas. Utilizing a high-resolution main ion charge exchange recombination spectroscopy system, the first characterization of edge deuterium temperature (T_D) and toroidal velocity ($v_{\phi,D}$) in a metal wall environment is presented. Dedicated experiments which examine the impact of the heating mix on T_D and $v_{\phi,D}$ in the ASDEX Upgrade tokamak are discussed. An unexpected temperature difference between main ions (T_D) and impurities (T_z) was discovered when increasing P_{ECRH}, $T_D > T_z$. The new temperature measurements have been used to solve the multi-ion heat transport equations with the ASTRA transport code. The interpreted deuterium (χ_D) and impurity (χ_z) heat diffusivities have been compared to fluid (TGLF) and gyrokinetic (GKW) models. While the dependence of a qualitatively similar χ_D/χ_z on the ion to electron heat flux (Q_i/Q_e) was identified in both experiment and simulation, discrepancies in the absolute value between the two are found when temperature differences between deuterium and impurities are present. The mechanism for the χ_D/χ_z dependence on Q_i/Q_e is the stronger resonant interaction of impurities with low drift frequency turbulence modes in comparison to deuterium. Importantly, it is shown that

---

[a] See Zohm *et al* 2024 (https://doi.org/10.1088/1741-4326/ad249d) for the ASDEX Upgrade Team.
[b] See Joffrin *et al* 2024 (https://doi.org/10.1088/1741-4326/ad2be4) for the EUROfusion Tokamak Exploitation Team.
[*] Author to whom any correspondence should be addressed.

1741-4326/25/096027+22$33.00 Printed in the UK

considering a single ion species (i), and assuming $T_D = T_z$ gives reasonable estimates of $\chi_D \approx \chi_i$ for the cases studied here. On the contrary, the evaluation of χ_z is very sensitive to ion temperature differences, which must be considered for accurate impurity ion heat transport description. Additionally, differences between $v_{\phi,D}$ and $v_{\phi,z}$ were compared to neoclassical calculations. Neoclassical theory can accurately describe $v_{\phi,D}$ (provided an independent measurement of $v_{\phi,z}$ or E_r) in the steep gradient region, but not at the pedestal top nor bottom, highlighting the complexity of edge transport phenomena.

Keywords: ion heat transport, deuterium temperature, neoclassical theory, main ion temperature, power balance analysis, ASTRA, TGLF

(Some figures may appear in colour only in the online journal)

---

1. Introduction

Understanding particle and energy transport is essential for the success of future fusion power plants. It will enable the optimization of plasma confinement, maximizing fusion power production and electricity output. Physics models that comprehensively account for relevant processes within the plasma need to be developed and validated against accurate measurements in current experimental devices for a reliable extrapolation towards next step devices. In particular, the study of transport in the main ion channel is crucial, as the main ions are responsible for fusion power production.

In the core of tokamak plasmas, performance is limited by turbulence. Temperature gradients are constrained to a critical threshold beyond which transport (heat diffusivity) increases drastically, leading to profile resilience. Profile stiffness has been experimentally observed in both the ion and electron channels [1, 2]. This phenomenon is well understood and attributed to the excitation of turbulence modes driven by thermodynamic forces (e.g. temperature gradients). In addition to turbulence, Coulomb collisions also lead to transport, which is described within neoclassical transport theory. The study of heat transport at the plasma edge of H-mode plasmas, and the mechanisms setting the pedestal top temperature, is vital. In this turbulence-suppressed region, higher gradients can be achieved, which enhance overall plasma performance.

Ion heat transport and flows have traditionally been studied by relying on minority (or impurity) ion species properties, due to the challenges associated with directly diagnosing the properties of the main ion species (in this work, deuterium). The strong collisional coupling between main ions and impurities justifies this assumption (see the appendix of [3]). Given their high mass, ions exhibit stronger coupling to each other than to electrons. This coupling limits temperature differences between species, which are constrained by thermal equipartition and transport mechanisms. Temperature differences may arise depending on factors such as the heating power scheme and plasma collisionality. Any potential discrepancies between main ion (T_D) and impurity (T_z) temperatures need careful quantification, particularly concerning their relevance in the context of ion heat transport studies.

Previous works which approximate the ion temperature to the impurity temperature have shown that ion heat transport at the plasma edge can be appropriately described by neoclassical models in H-mode plasmas at AUG [4–6] and LHD [7]. In other edge turbulence suppressed confinement regimes, such as QH-mode, the edge ion heat transport can be properly described using neoclassical models [8] accounting for extended effects [9, 10]. Studies in the core [11] and edge [12] of DIII-D H-mode plasmas indicate that the neoclassical values may be even too large to describe ion heat transport in the pedestal region.

Recent advances in modeling and diagnostic techniques have made the direct diagnosis of deuterium temperature possible [13, 14]. A recent study at the DIII-D tokamak, utilizing state-of-the-art main ion measurements ($T = T_D$), reports ion heat transport coefficients at the edge well above the neoclassical values for low ITER-like collisionality (ν_i^*) H-mode plasmas [15]: at low ν_i^*, ion scale electrostatic turbulence can have a bigger contribution to the total ion heat flux than neoclassical transport. In these experiments, $T_z > T_D$. This result is in contrast with previous inter-ELM H-mode results from AUG (which used $T = T_z$), which report good agreement with the neoclassical heat conductivity across a ν_i^* scan ($\nu_i^* = [0.20, 2.45]$) and varying ECRH power deposition [5].

This work addresses the study of ion heat transport and flows using an experimental characterization of deuterium temperature and toroidal velocity in H-mode plasmas at the AUG tokamak. The measurements have been taken with a dedicated main ion charge exchange recombination spectroscopy system, which is described in section 2. The experimental temperature profiles are presented in section 3, including a consistency check of the new measurements and a comparison of T_D, T_z and electron temperature (T_e) profiles for an ECRH power scan. The temperature profiles are evaluated doing power balance analysis to determine the interpretive heat transport coefficients, which are compared to theoretical models in section 4. The new deuterium toroidal velocity profiles and a comparison to neoclassical models is discussed in section 5. The conclusions drawn from this work, as well as directions for future work, are presented in section 6.

2. Methodology

In this work, the main ion [16] and impurity [17, 18] temperatures are measured using Charge Exchange Recombination Spectroscopy (CXRS). The results presented here correspond to inter-ELM H-mode plasmas. In this section, the experimental setup, the workflow for the interpretation of main ion spectra and the plasma scenarios are described.

2.1. The experimental setup

The edge main ion diagnostic is a CXRS diagnostic which relies on the detection of thermal deuterium emission after a charge exchange (CX) reaction. The main ion charge exchange diagnostic (MICX) provides beam-based CXRS measurements using a 93 keV heating beam (beam source Q8). This system is described in [16], and since this publication the MICX diagnostic has been upgraded with a new in-vessel optical head with 30 lines of sight (LOS), that enable measurement of the main ion and impurity spectra in the same measurement volume using two spectrometers. A subset of 15 LOS is used for the main ion system, covering 6.5 cm in the edge region (from pedestal top to separatrix) with a spatial resolution down to 3 mm. The standard temporal resolution is 1.5 ms for the 15 LOS (it can be tuned down to μs if only one LOS is imaged on the camera chip [19]). The high spatio-temporal resolution is essential for resolving the fast dynamics and steep gradients present at the plasma edge of H-mode plasmas. The optical head features $f/2.7$ plano-convex lenses with a focal length of 85 mm, and is a replica of the edge toroidal optical head installed in sector 15 for impurity measurements which uses a 60 keV heating beam (beam source Q3) [18]. A toroidal and poloidal view of the diagnostic optics and beam geometries are shown in figures 1(*a*) and (*b*), respectively.

The impurity temperature, toroidal and poloidal velocity profiles have been measured with dedicated impurity systems, also shown in figures 1(*a*) and (*b*). In this work, the impurity and main ion measurement volumes are located in different toroidal sectors, with T_D and T_z measurements conducted on a 93 keV (Q8) and a 60 keV (Q3) beam source, respectively.

In addition, the edge main ion diagnostic has also been upgraded with a geometrical parabolic filter. The filter is installed in front of the camera chip to block the intense cold D_α light, following the approach detailed in [19]. The parabolic shape improves the efficient blockage of the emission from the cold neutrals at 656.1 nm for all fibers imaged on the camera chip, as there is a parabolic shift of the central wavelength in the vertical direction [20].

Note that all impurity profiles presented in this work refer to B^{5+}. To ensure good impurity CXRS signal, all the discharges are performed close to boronization. At least one gyrotron is switched on to avoid tungsten accumulation. The effective charge (Z_{eff}) has been determined experimentally by the Bremsstrahlung level and is between 1.4 and 1.5 for all discharges.

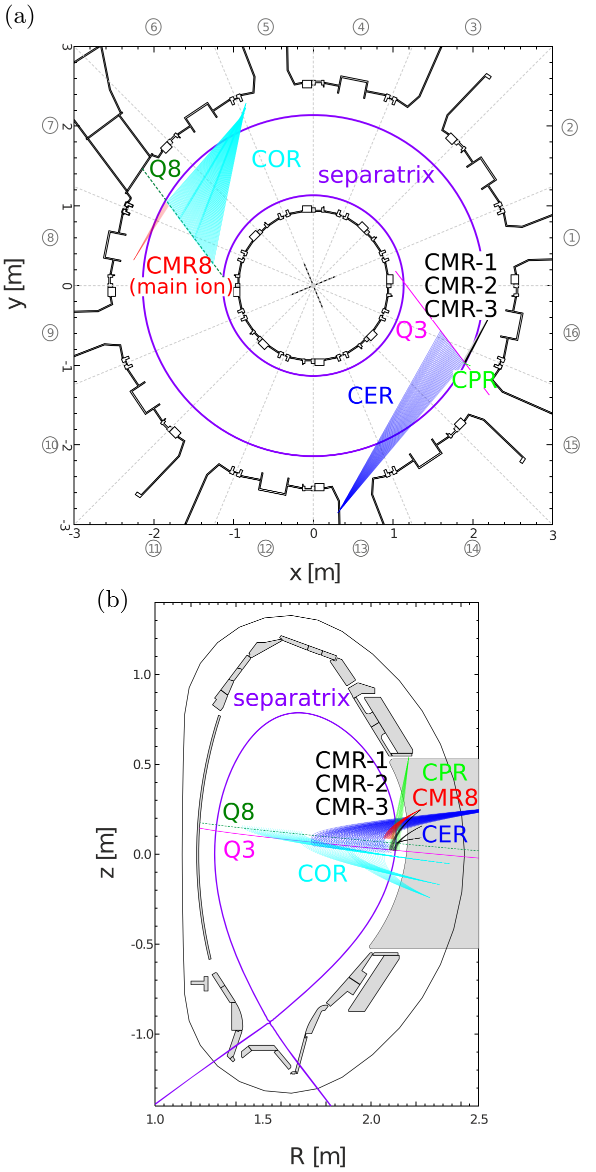

Figure 1. (*a*) Toroidal and (*b*) poloidal view of the Charge Exchange Recombination Spectroscopy diagnostics at the ASDEX Upgrade tokamak and the Neutral Beam Injection sources. The NBI source Q3 is the diagnostic beam for the toroidal core and edge systems (CER and CMR-1 to CMR-3) and edge poloidal (CPR) system, while the NBI source Q8 is the diagnostic beam for the core and edge toroidal systems (COR and CMR-8).

2.2. Analysis of main ion spectra

For many years, the multiple photoemission processes involved in the deuterium spectra and spectral overlap have prevented the analysis of main ion spectra for the direct determination of main ion profiles. Figure 2 shows the total (black), active (red) and passive (blue) main ion spectra. In the absence of an active source of neutrals, in this work, the NBI Q8, the main ion spectrum is purely passive (blue spectra in figure 2). The passive spectra consists of a cold and a thermal D emission, as well as the carbon II lines. The passive D emission

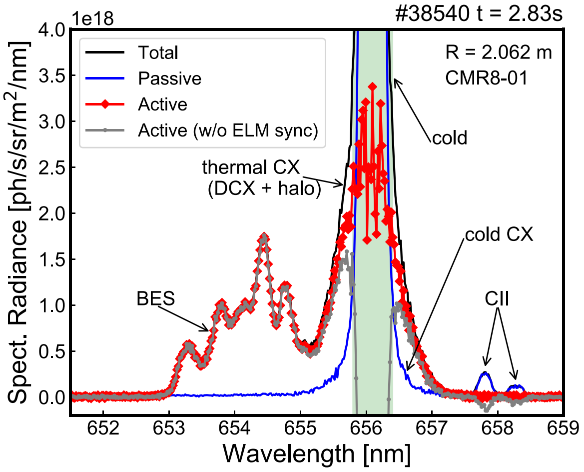

Figure 2. Total (diagnostic beam on, black), passive (diagnostic beam off, blue), and an active spectra with (red) and without (gray) ELM synchronization are shown. The shaded green area indicates the region attenuated by the wire shadow.

is due to excitation of background neutral deuterium atoms (labeled as cold in figure 2) and CX reactions between thermal D ions and the background neutral deuterium (labeled as cold CX in figure 2). These emissions are line integrated and not localized. When an active source of neutrals is provided, in this case, the Q8 beam source is switched on, mainly two features appear in the spectra: the thermal active emission (active thermal CX, consisting on both DCX and halo) and the beam emission (BES). The active thermal D emission is of interest for this work, as it contains localized information on the main ion temperature (T_D) and toroidal velocity ($v_{\phi,D}$). In order to isolate the active (localized) emission from the total spectra, the passive contribution to the spectra has to be removed. Modeling the passive deuterium spectra is complicated due to the large uncertainties in the background neutral deuterium density profiles and its 3D structure [21, 22]. For this reason, passive background subtraction is an important part of the main ion spectral analysis, as will be discussed in this subsection.

The main issues for the routine analysis of main ion spectra are [13]: (i) Thermal halo emission from multiple CX reactions, which enhances line integration effects and compromises the resolution of the diagnostic technique. (ii) Smearing due to single-charge main ion species. Since D only has one proton, the deuterium ion becomes neutral after the CX reaction. As a neutral, D does not feel the magnetic field and travels ballistically, such that diffusion across flux surfaces is enhanced. (iii) Bright emission from cold neutrals at the plasma edge, which can lead to malfunctioning or damage of the instrumentation (camera saturation) and prevent the feasibility of the measurement. (iv) Cross-section distortions due to the energy dependence of the CX reaction rate. (v) The finite lifetime of excited states. (vi) Spectral overlap, such as with BES, in the same wavelength range.

In recent years, developments in CCD diagnostics, comprehensive spectral fitting and code development for the modeling of the main ion spectra have enabled the feasibility of main ion CXRS analysis [13, 14, 23–27].

In this subsection, the forward model and data analysis tools employed for a successful interpretation of the spectra are presented. The forward modeling framework corrects for the halo, line integration and cross-section distortions. Comprehensive passive background subtraction, that considers ELM synchronization, enables the elimination of the passive contributions to the main ion spectra and enables the comparison of the experimental and synthetic spectra.

2.2.1. Forward model. The core of the forward modeling framework is the collisional-radiative model included in the FIDASIM4 code [28, 29], following the approach in [26]. Given an assumption on the T_D, n_D and $v_{\phi,D}$ profiles, FIDASIM4 computes the synthetic spectra, using the magnetic equilibrium reconstruction, beam and diagnostic geometries. In this work, FIDASIM4 has been used to model the active thermal CX (both DCX and halo) and BES contributions to the main ion spectra. It has been verified that the contribution of the FIDA emission to the spectra is negligible for these cases, and is only important for low density plasmas with strong off-axis NBI heating [30, 31]. The synthetic spectra are fitted to obtain synthetic apparent T_D and $v_{\phi,D}$ profiles, which are compared to the experimental apparent T_D and $v_{\phi,D}$, obtained from fitting the active experimental spectra. A correction factor is defined from the comparison of the synthetic and experimental apparent profiles, which is used to modify the input profiles to FIDASIM4 in an iterative process. The true underlying main ion properties are resolved when the synthetic and experimental profiles and spectra match within uncertainties. More details on the work-flow are given in [16].

Importantly, FIDASIM4 is used within the iteration process to compute the effective diagnosed region for each LOS. FIDASIM4 stores the birth positions of neutrals that emit photons leading to D$_\alpha$ radiation intersecting a LOS [32]. Figure 3(a) shows the birth location's distribution of neutrals that emit a photon intersecting the innermost (CMR8-01) and outermost (CMR8-16) LOS. These distributions are used to compute a histogram as a function of the radial coordinate, which can be seen in figure 3(b). These histograms are fitted using a Gaussian function (which can be seen in transparent dashed lines). The center and spread of the histogram are used to calculate the measurement location (R) and spatial resolution (σ_R), respectively. The resolution σ_R has been calculated as the FWHM of the Gaussian fit. Figure 3(c) shows the resolution for each LOS as a function of its measurement location. These birth maps have been used to map the experimental profiles to magnetic coordinates. Note that the resolution in the pedestal region is down to 4 mm, while for LOS further in the spatial resolution is compromised, due to the loss of tangency to the flux surfaces.

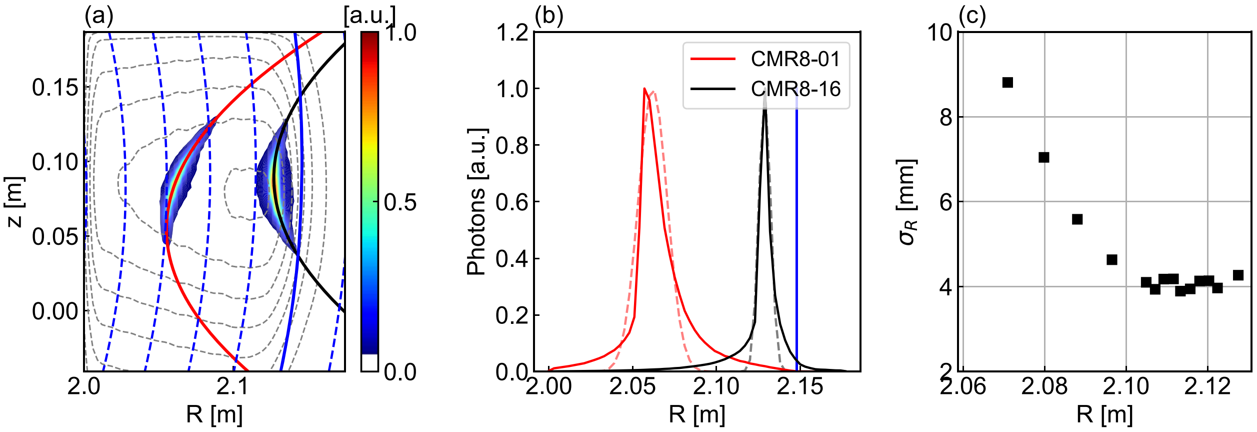

Figure 3. (*a*) Birth distribution of neutrals which emit a photon intersecting the inner (red) and outermost (black) lines of sight, (*b*) corresponding radial histograms (solid) and a Gaussian fit (dashed) to the histograms, and the separatrix location (blue) and (*c*) the radial resolution (σ_R) as a function of the centre of the radial histograms (R), which gives the measurement position.

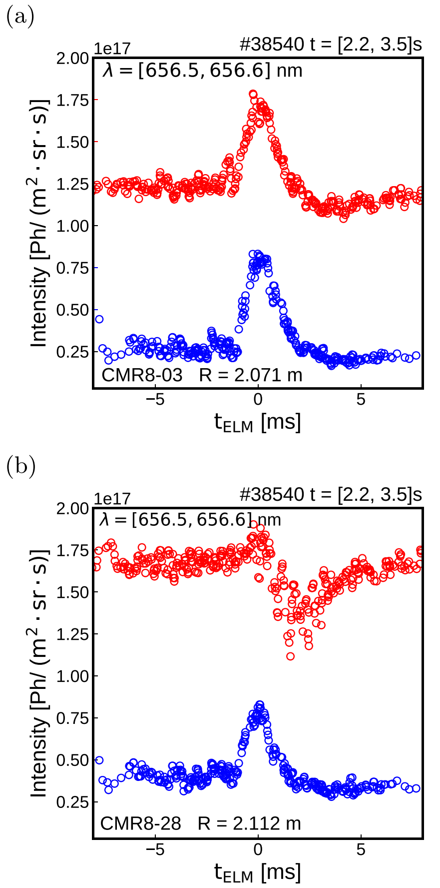

Figure 4. Temporal evolution of the active (red) and passive (blue) main ion spectra (for an integrated wavelength range of $\lambda = [656.5, 656.6]$ nm) with respect to the ELM onset for an (*a*) inner and (*b*) outer line of sight.

2.2.2. Background subtraction and ELM synchronization.

As previously explained, the passive contribution to the spectra has to be removed to compare the active experimental and synthetic spectra computed by FIDASIM4. Unless specified otherwise, in all analyzed discharges Q8 (main ion diagnostic beam) and Q3 (impurity diagnostic beam) are alternated, using a duty cycle of 60 ms on and 40 ms off for Q8 and opposite modulation for Q3. In this way, active and passive frames are collected and beam power is compensated. In order to do background subtraction, the assumptions that the background neutral density at the measurement location does not depend on which NBI source is being used and that there are no significant differences in the main plasma parameters between the active and the passive time windows, have to be made, and the ELM dynamics have to be included to properly substract the data. Figures 4(*a*) and (*b*) show the temporal evolution of the D_α radiance during an ELM cycle for two LOS. Here, the signal for $\lambda = [656.5, 656.6]$ nm has been integrated and synchronized with respect to the ELM onset for a stable time window $t = [2.2, 3.5]$ s in discharge #38540. The passive and active signal are shown in red and blue, respectively. It can be seen that the active and passive signals for both LOS are clearly modulated during the ELM cycle: for the inner LOS, the active and passive signals rise during the ELM crash, while for the outer LOS the active signal collapses during the ELM. All signals return to their pre-ELM values within 4 ms after the ELM crash. To eliminate the impact of the ELM on the main ion spectra, it is crucial to ELM-synchronize both the passive and the active spectra to guarantee efficient background subtraction. Figure 2 further illustrates the importance of ELM-synchronization. This figure shows an example of ELM-synchronized background subtraction in red and non-ELM-synchronized background subtraction in gray (which uses the closest passive frame to the active frame). It can be seen that when ELM-synchronization is implemented, the CII and cold passive emissions are effectively removed. In contrast, without ELM synchronization residual cold and carbon emissions are visible in the spectra. This provides a consistency check that the plasma parameters are matched in the ELM-synchronized passive and active frames. All the data presented in this work has been ELM-synchronized and correspond to a time window of $t = [-4, -2]$ ms with respect to the ELM crash. The passive emission is also important because it limits the extension of beam-based main ion measurements towards the separatrix and SOL. In a metal wall machine, the passive emission surpasses the active emission as the separatrix is approached, leading to low signal-to-noise ratio, and making the measurement impractical. Future work will focus on diagnostic development that focuses on measuring main ion properties at the separatrix and in the SOL.

In addition to the ELM synchronized passive background subtraction, during other steps of spectral analysis, corrections and assumptions need to be made which could affect the final main ion profiles. These possible sources of uncertainty include the assumption on the plasma hydrogen content, the definition of the wavelength of interest for the fit and the uncertainty in the intensity calibration. Their impact on the main ion profiles, in the view of the results presented in section 3, are addressed in the appendix.

2.3. Experiment description

The experiments were designed to study the impact of input power and collisionality on T_D and $v_{\phi,D}$. In total, four lower single null deuterium H-mode plasma discharges were executed (favorable configuration, $B_t = -2.5$ T). Both NBI and ECRH input power were used as actuators to affect the temperature profiles and collisionality, with the expectation that increasing plasma heating and lowering the collisionality, could lead to a less efficient heat transfer between the ion species and, therefore, a decoupling between main ion and impurity temperature. In addition, a change in the friction forces between the main and impurity ions across different collisionality regimes would allow us to characterize the ion flows and the differential ion toroidal rotation, and document whether the collisionality regime has an impact on the nature of ion toroidal rotation at the edge region.

An overview of the experiments is given in figures 5(*a*)–(*c*), which show (*a*) the ECRH input power (P_{ECRH}), (*b*) the line integrated edge electron density ($\bar{n}_e$) and (*c*) the NBI input power (P_{NBI}). Each discharge is divided into 3 phases, highlighted in shades of gray. Discharges #38539, #38540 and #38587 feature a 2.5 MW step-wise increase of P_{NBI} by including an additional NBI source in each phase, while the P_{ECRH} remains constant (note that in the beginning of the third phase discharge #38539 terminates and #38540 loses one gyrotron). Here, P_{ECRH} is scanned from one discharge to another. The minimum (maximum) P_{ECRH} is 0.7 (3.8) MW, corresponding to 1 (5) gyrotrons.

In discharge #39000, P_{NBI} is constant (one source) and P_{ECRH} is changed. This discharge provides two intermediate P_{ECRH} cases. Here, beam compensation of NBI source Q8 is done with NBI source Q6, and the impurity measurements are taken during steady phases with source Q3 only.

An overview of the relevant plasma parameters is given in table 1. In these discharges, the Pfirsch-Schlüter collisionality limit is at $\nu_* \sim 7.0$ ($\nu_* = 6.7 - 7.4$), and the banana limit is at $\nu_* = 1$. The plasma line integrated density ($\bar{n}$) is fairly constant across all plasma discharges, as shown in figure 5(*b*). In #38587, the plasma current (I_p) was increased to $I_p = 1.0$ MA, resulting in the higher density in this discharge as can be seen in figure 5(*b*). The total power and stored energy change throughout the discharges (P_{tot} varies from 3.5 to 11 MW). The radiated power (P_{rad}) also changes in steps and proportionally to the stored energy (P_{rad} varies from 1.5 to 3.5 MW). A low ELM frequency is targeted to facilitate ELM synchronization of the data. However, the increase of input power unavoidably leads to an increase of the ELM repetition time.

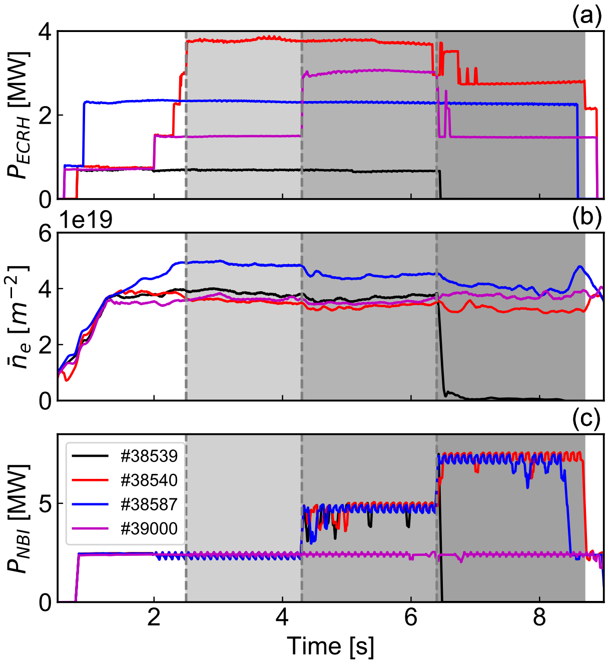

Figure 5. Time traces for the discharges of interest: (*a*) total ECRH input power (P_{ECRH}), (*b*) line integrated edge electron density ($\bar{n}$) and (*c*) total NBI input power (P_{NBI}).

The NBI and ECRH power deposition have been modeled using the ASCOT [33] and TORBEAM codes, respectively. The ECRH power is deposited only on the electrons and in the core. The NBI power is split collisionally between the ions and the electrons depending on the local density and temperature and fast particle energy [34]. The NBI power deposition per particle is higher for impurities than for main ions, which has important implications for the calculation of heat diffusivities, as will be shown in section 4.

3. Experimental temperature profiles

In this section, the first edge deuterium temperature (T_D) measurements at the ASDEX Upgrade tokamak are presented. The main ion temperature is compared to the impurity (T_z) and electron (T_e) temperature profiles.

3.1. Consistency check

First, the consistency of the methodology is presented. The T_D, T_z and T_e profiles at medium collisionality ($\nu_{*,i}^{\mathrm{ped.\ top}} = 1.5$) and low ELM frequency ($f_{\mathrm{ELM}} = 60$ Hz) are shown in figure 6(*a*) in red, gray and blue, respectively. The temperatures are in

Table 1. Relevant parameters for the H-mode discharges: plasma current (I_p), safety factor at $\rho_{\mathrm{pol}} = 0.95$ (q_{95}), Pfirsch-Schlüter collisionality limit ($\nu_{*,i,\mathrm{PS\ limit}}$) and NBI sources besides diagnostic beams Q3 and Q8.

	I_p (MA)	q$_{95}$	$\nu_{*,\mathrm{i,PS\ limit}}$	Extra NBI sources
#38539	0.8	5.3	7.4	Q5
#38540	0.8	5.2	7.4	Q5, Q6
#38587	1.0	4.3	7.0	Q2, Q6
#39000	0.8	5.4	6.7	N/A

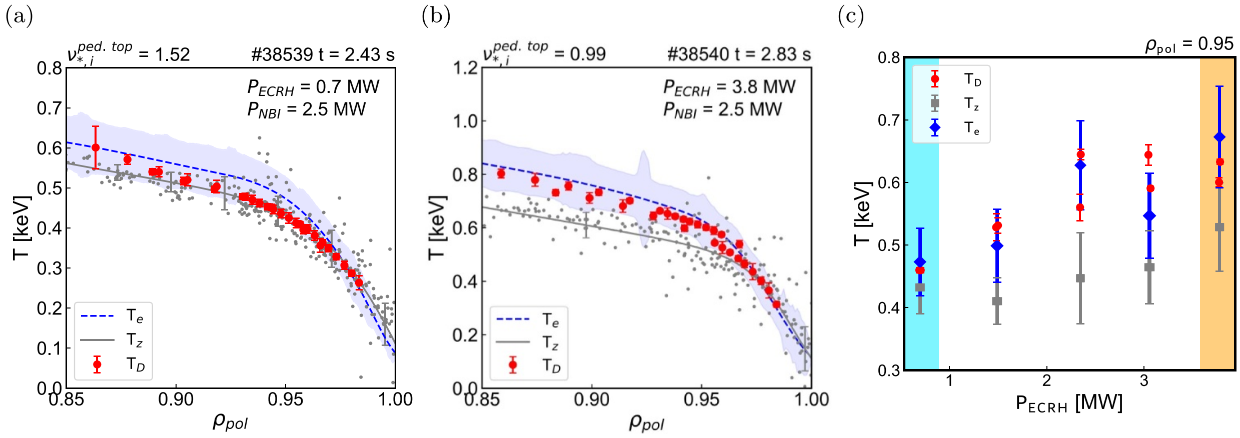

Figure 6. Experimental electron (blue), main ion (red), impurity (gray) temperature in (a) the *plateau* regime ($\nu_{*,i}^{\mathrm{ped.top}} = 1.5$, $P_{\mathrm{ECRH}} = 0.7$ MW) and (b) the banana limit ($\nu_{*,i}^{\mathrm{ped.top}} \sim 1.0$, $P_{\mathrm{ECRH}} = 3.8$ MW). For clarity, a few errorbars are shown for the T_D and T_z profiles, while the T_e errorbar is shown in a shade of blue. (a) and (b) correspond to the cases highlighted in orange and blue. (c) Experimental main ion (red), impurity (gray) and electron (blue) pedestal top temperature as a function of input P_{ECRH} in (c), respectively. Please note the extended corrections (mainly, due to a H contribution to the spectra) are not included here.

good agreement within the experimental uncertainties (errorbars and uncertainties in mapping of profiles), which indicates that all species are in thermal equilibrium. Please note that the T_D profiles shown in figures 6(a)–(c) have been evaluated at two different outer plasma radius (R_{out}) positions to increase the radial coverage, while all other plasma parameters are kept constant. The evaluation of T_D at two different time points provides an additional measure of the accuracy of the analysis, illustrated by the scatter between the two profiles. In this case, the profiles for the two R_{out} positions perfectly overlap. In addition, T_D is shifted –2 mm, which is within the radial resolution of the diagnostic. The fact that $T_D = T_z$ is consistent with the local ion equilibration time being short compared to the transport time scale [17]. As will be shown in section 5, the difference between main ion and impurity edge toroidal velocity is consistent with neoclassical transport theory.

3.2. Scan of electron heating

The impact of varying P_{ECRH} at constant NBI input power ($P_{\mathrm{NBI}} = 2.5$ MW) is examined. The ECRH power is varied in 5 steps from 0.7 to 3.8 MW, which leads to a $\nu_{*,i}^{\mathrm{ped.\ top}}$ that varies from 1.52 to 1.0 (from *plateau* to banana limit collisionality regimes). Figure 6(c) shows an overview of the pedestal top ($\rho_{\mathrm{pol}} = 0.95$) temperatures as a function of P_{ECRH} (please note that here the double points for each P_{ECRH} correspond to the two R_{out} positions). At low input power ($P_{\mathrm{ECRH}} = 0.7$ MW, highlighted in cyan), the three species are in thermal equilibrium (this case corresponds to the consistency check presented in figure 6(a)). While T_D, T_e and T_z increase with input power, T_z increases at a slower rate than T_D and T_e. Therefore, main ions and impurities are well coupled at lower power (and higher collisionality), but the difference between them increases with P_{ECRH}, until it saturates at approximately 2.5 MW. On the contrary, the main ion and electron temperatures are well coupled across the full ECRH scan. Note that a similar trend is found for the evolution of T_D, T_z and T_e across the P_{ECRH} scan inside the pedestal top ($\rho_{\mathrm{pol}} = 0.90$), while in the steep gradient region the main and impurity ions are found to be in thermal equilibrium within the experimental uncertainty across the ECRH power scan.

Figure 6(b) shows the detailed temperature profiles for discharge #38540 at $t = 2.83$ s, which corresponds to the maximum P_{ECRH} case in figure 6(c), highlighted in orange. In this case, the three species are in thermal equilibrium ($T_e = T_D = T_z$) in the steep gradient region ($\rho_{\mathrm{pol}} = 0.98$). As the pedestal top is approached, approximately $\rho_{\mathrm{pol}} = 0.95$, T_D and T_z decouple. Interestingly, T_D closely follows T_e at the pedestal top and inside the pedestal top. This is an unexpected observation, as the main ions and impurities are expected to be collisionally coupled and in closer thermal equilibrium due to a stronger and faster ion thermal equilibration time compared to electrons [35]. Differences between T_D and T_z have also been reported at the DIII-D tokamak [15]. However, results from

DIII-D reveal a temperature difference towards the separatrix, and not towards the pedestal top. In addition, when a temperature discrepancy is observed, T_z is larger than T_D, while the opposite ($T_D > T_z$) is reported here for AUG at the pedestal top. Also in contrast with AUG results, an inter-species power balance analysis carried out in JET reports that impurity temperatures can be 5%–10% higher than the main ion temperature [36].

3.3. Extended corrections to the T_D profile

Within the experimental uncertainty, $T_D = T_z$ in the steep gradient region, but T_D is 100 eV higher than T_z in the pedestal top. The temperature differences reported in this study are outside the errorbars when standard main ion analysis (described in section 2.2) and corrections are applied. However, extended corrections and sources of uncertainty, which could bring the main and impurity temperature profiles to closer agreement, have been considered and examined in this work, and are described in detail in the appendix. The main correction comes from including a H contribution to the D spectra (which for the concentration values in this campaign, would lead to a maximum 4% reduction of the T_D profile), and the secondary correction is due to line of sight integration effects for the impurity spectral analysis (which brings up T_z at the pedestal top by approximately 10 eV). When these are included, the difference between the T_D and T_z in the pedestal top is reduced to 50–60 eV in discharge #38540. As discussed in further detail in the appendix, a 50–60 eV temperature difference could be explained by accumulative uncertainties stemming from various stages in the spectral analysis. Nevertheless, the observation of $T_D > T_z$ at the pedestal top in discharge #38540 is not an isolated case, but has been noted in different plasma scenarios, alongside cases where $T_D = T_z$ is also documented. These findings give confidence to the authenticity of the trend. In addition, applying these corrections to discharge #38539, the case with minimum ECRH heating shown in figure 6(*a*), gives T_D and T_z still in thermal equilibrium. In comparison, making this correction to the case with maximum ECRH heating, shown in figure 6(*b*), still gives a temperature difference between T_D and T_z of 60 eV. Even when applying the extended corrections, the trend of seeing a temperature separation with increasing electron heating fraction is robust. In the light of these results, the implications of a temperature difference between main and impurity ions for ion heat transport studies are discussed in detail in section 4.

4. Multi-ion species heat transport analysis

This work provides new insights in the field of ion heat transport studies, as it uses the new main ion temperature measurements to account for differences in the ion temperature profiles for each species to achieve a comprehensive characterization of ion heat transport. To properly address this, multi-ion heat transport analysis is carried out, by consistently and simultaneously solving the ion heat transport equation for main ions and impurities. To fulfill this purpose, the ASTRA code [37, 38] is used, which enables the implementation of the ion heat transport equation for each ion species independently.

The results from interpretive (power balance analysis) and predictive modeling are presented in sections 4.1 and 4.3, respectively. ASTRA simulations have also been compared to turbulence models in section 4.2.

The heat flux (Q_α) is determined from the energy balance equation for species α, considering transport in the radial direction (across flux-surfaces) under the assumption of purely diffusive heat transport, and is given by:

$$Q_\alpha = -n_\alpha \chi_\alpha \frac{\partial T_\alpha}{\partial \rho} \frac{\partial V}{\partial \rho} \langle (\nabla \rho)^2 \rangle, \tag{1}$$

where n_α is the density, T_α the temperature and χ_α is the heat conductivity or diffusivity. Consequently, the heat conductivity (χ_α) for a plasma species α is computed as:

$$\chi_\alpha = -\frac{Q_\alpha}{n_\alpha (\partial T_\alpha / \partial \rho) \langle (\nabla \rho)^2 \rangle (\partial V / \partial \rho)}. \tag{2}$$

Note that Q_α is the volume integral of the energy sources, or power density P_α, $Q_\alpha = \int P_\alpha \, \mathrm{d}V$. The power deposition into each plasma species, namely electrons, main ions (deuterium) and impurity ions (boron), considers:

$$P_e = P_{\mathrm{Oh}} + P_{\mathrm{ECRH}} + P_{\mathrm{NBI},e} + P_{D,e} + P_{z,e} - P_{\mathrm{rad}} \tag{3}$$

$$P_D = P_{\mathrm{NBI},D} + P_{e,D} + P_{z,D} \tag{4}$$

$$P_z = P_{\mathrm{NBI},z} + P_{e,z} + P_{D,z} \tag{5}$$

where $P_{\mathrm{NBI},\alpha}$ is the power transferred from the NBI particles to bulk plasma species α via collisions, P_{ECRH} is the electron cyclotron heating, P_{oh} is the ohmic heating, P_{rad} is the radiated power and $P_{\alpha,\beta}$ is the collisional heat exchange term from the plasma species α to the plasma species β, and so $P_{\alpha,\beta} = -P_{\beta,\alpha}$. Note that the heat transport equations are coupled via these heat exchange terms. The heat exchange term $P_{\alpha,\beta}$ between the plasma species α and β has been calculated as [35, 36, 39]:

$$P_{\alpha,\beta} = c_{eq} \Lambda_{\alpha\beta} n_\alpha n_\beta \frac{(A_\alpha A_\beta)^{1/2} (Z_\alpha Z_\beta)^2}{(A_\alpha T_\beta + A_\beta T_\alpha)^{3/2}} (T_\alpha - T_\beta) \tag{6}$$

where c_{eq} is $3.26 \times 10^{-32}\,\mathrm{W\,eV^{1/2}\,m^3}$, Λ is the Coulomb logarithm [40] and A and Z are the mass and atomic number, respectively. Please note that fully ionized deuterium and boron ions are more strongly coupled than main ions and electrons by a factor of $\sqrt{m_D/m_e}$. Importantly, a small temperature difference between deuterium and boron leads to a strong heat exchange term, which should lead to fast thermal equilibration between ion species. This is illustrated in figure 7, which shows the heat flux from deuterium

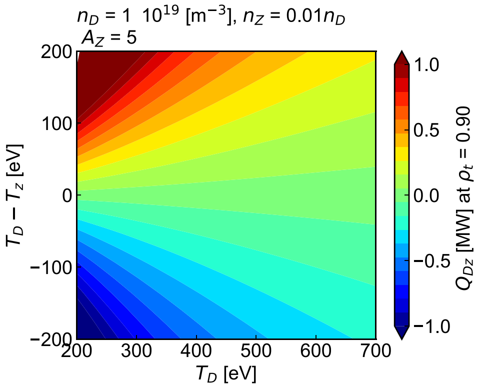

Figure 7. Heat flux induced at $\rho_{\mathrm{tor}} = 0.9$ by thermal heat exchange (equipartition) between main ions (D) and impurities (B) assuming $n_D = 10^{19}$, $n_z = 0.01n_D$, assuming a constant power transfer across full radial profile calculated from equation (6) as a function of T_D and the temperature difference $T_D - T_z$.

($A_\alpha = 1$, $Z_\alpha = 2$) to boron ($A_\beta = 5$, $Z_\beta = 10$) at $\rho_{\mathrm{tor}} = 0.9$ as a function of the deuterium temperature and $T_D - T_z$. For the calculation, it has been assumed that $n_\alpha = 10^{19}$ m^{-3}, $n_\beta = 0.01n_\alpha$ and that $P_{\alpha\beta}$ is constant across the full plasma radius. As can be seen, large heat fluxes are driven by small tempeture differences (e.g. a temperature difference of 50 eV at $T_D = 200$ eV gives a 0.5 MW heat flux).

Here, $P_{\mathrm{NBI},\alpha}$ has been calculated by means of the ASCOT code [33]. ASCOT is a Monte Carlo orbit following code that calculates the power deposited to each plasma species for realistic NBI geometry and energy and experimental equilibrium and plasma profiles. The ECRH power deposition is modeled with the TORBEAM module in ASTRA. The experimental radiated power profile, as reconstructed from the bolometer signals, is used for the simulations. The main ion and impurity density profiles are estimated according to quasineutrality ($n_e = n_D + Z_z n_z$) and using the experimental effective charge Z$_{\mathrm{eff}}$, where Z$_{\mathrm{eff}} = (\sum n_\alpha Z_\alpha^2)/n_e$. It has been verified that the use of experimental impurity density profiles, as diagnosed by CXRS, has a negligible impact on the calculation of χ_z and χ_D.

An example of the NBI power density deposition, which is the power per particle $p_{\mathrm{NBI},\alpha} = P_{\mathrm{NBI},\alpha}/n_\alpha$, as calculated by ASCOT is shown in figure 8. The ratio of the NBI power density deposition to impurities ($p_{\mathrm{NBI},z}$) divided by the NBI power density to the main ions ($p_{\mathrm{NBI},D}$) is shown in the right axis in figure 8 for boron, carbon and nitrogen. Note that as collisions scale with the particle charge, the boron impurities receive 5 times more power than the main ions per particle. This is also true for the heat exchange between the thermal plasma species, i.e. $P_{e,Z}/n_Z \propto ZP_{e,D}/n_D$. The implications are discussed in the next subsection.

4.1. Interpretive power balance analysis

Interpretive analysis consists of the determination of the heat diffusivities (χ_α), when the temperature (T_α) and heat flux (Q_α) profiles are inputs. Note that Q_α is here an input as it can be calculated as the volume integrals of P_α, following equations (3)–(5) (the details on the calculation of the different contributions to P_α for each plasma species can be found in the previous subsection). The heat transport is inferred by adjusting χ to match the evolution of the experimental profiles. The analysis has been applied to the lowest and highest P_{ECRH} cases within the power scan presented in figure 6(*c*).

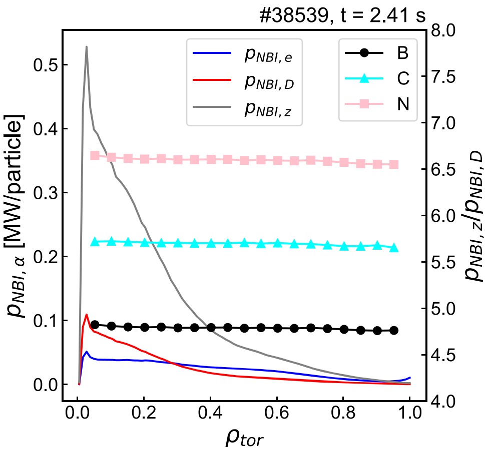

Figure 8. NBI power density ($p_{\mathrm{NBI},\alpha} = P_{\mathrm{NBI},\alpha}/n_\alpha$) deposition to electrons (blue line), main ions (red line) and impurities (gray line) for #38539 as calculated with the ASCOT code on the left axis. On the right axis, the ratio of the NBI power deposition per particle to impurities with respect to the main ions ($p_{\mathrm{NBI},z}/p_{\mathrm{NBI},D}$) for different impurity species (symbols).

First, the reference case in which the ions are in thermal equilibrium within the experimental uncertainty ($T_D = T_z$, #38539, see figure 6(*a*)) is investigated. This case constitutes the ideal limit, in which T_D is identically equal to T_z, therefore the two temperature profiles, input to the simulation, are equal, as can be seen in figure 10(*a*). Figures 9(*a*)–(*c*) show the contributions and total power density to the main ions, impurities and electrons, respectively. As the main ion and impurities are in thermal equilibrium, the ion heat exchange power is zero ($T_D - T_z = 0 \rightarrow P_{D,z} = 0$). The power input to the main ions and impurities are due to collisions with the NBI and with electrons and, for both contributions, the heat deposition per particle is 5 times larger for impurities. This is why P_z is 10 times smaller than P_D, despite n_z being 100 times smaller than n_D. For the electrons, the input power is dominated by ECRH heating. In reality, as soon as T_D slightly deviates from T_z, a large heat flux develops from one species to the other (see figure 7), which in combination with the transport levels for the two ion species, would prevent the two temperatures to develop a measurable difference (a situation with different T_D and T_z profiles will be discussed later).

Figure 10(*b*) shows the integrated heat fluxes, i.e. the volume integrals of the black profiles shown in figures 9(*a*)–(*c*). The main ion and electron heat fluxes are comparable, and a factor of 9 larger than the impurity heat flux. The resulting heat diffusivities and neoclassical calculations [41, 42] are shown in figure 10(*c*). Interestingly, $\chi_z \sim 4.8\chi_D$. This factor is a consequence of the collisional heat transfer (from both

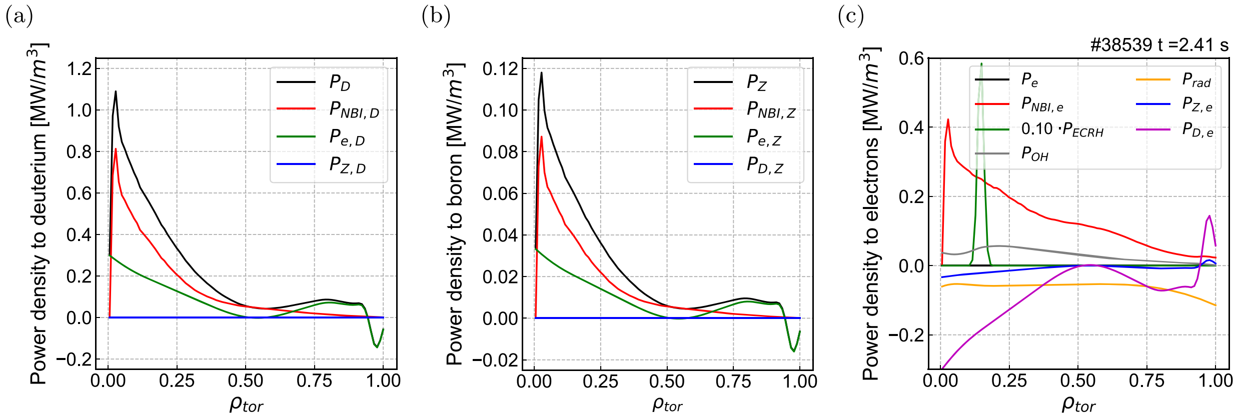

Figure 9. Power density profiles for (a) the main ions, (b) impurities and (c) electrons for discharge #38539. The individual contributions and sum, as stated in equations (3)–(5), are shown. The main ion to impurity heat exchange term ($P_{D,z}$) is zero, as $T_D = T_z$ (see figure 10(a)).

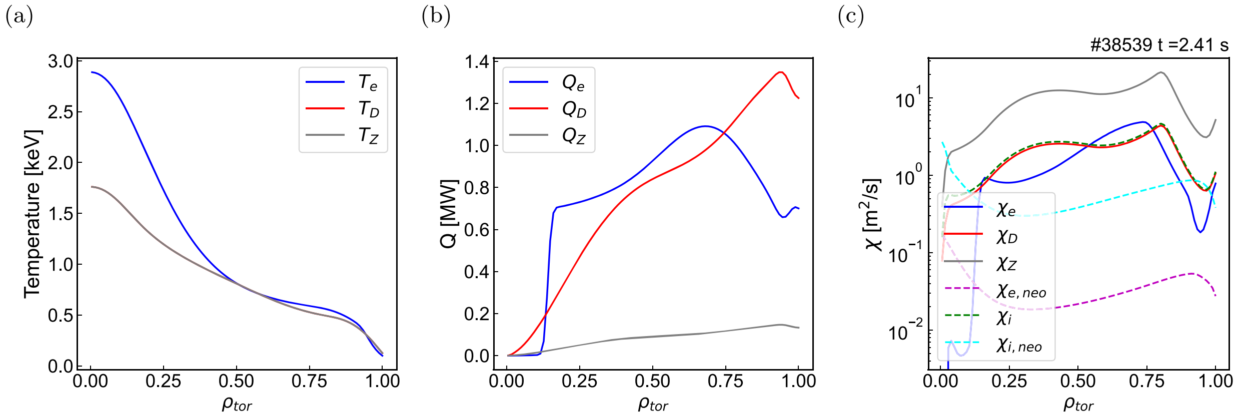

Figure 10. Main ion (red), impurity (gray) and electron (blue) (a) temperature profiles used as input for ASTRA simulations, (b) heat fluxes and (c) heat diffusivity radial profiles. The effective ion (green), and the neoclassical ion (cyan) and electron (magenta) heat diffusivities are also shown.

NBI and electrons) being a factor of 5 larger for boron than for deuterium (as shown in figure 8). While the main ion heat flux is almost one order of magnitude higher, the main ion density is much larger than the impurity density (in this case, $n_z \sim 0.023 n_D$), which according to equation (2), leads to $\chi_z > \chi_D$. It can be seen that χ_D is close to the neoclassical value in a narrow region in the steep gradient region, while $\chi_{i,\mathrm{neo}}$ is too low in the pedestal top and bottom. In contrast, $\chi_e > \chi_{e,\mathrm{neo}}$ across the entire radius. Both results are in agreement with previous works [17]. The effective ion heat diffusivity (χ_i), which uses the ion temperature (in this case, $T_i = T_D = T_z$), ion density ($n_i = n_D + n_z$) and total NBI power density to the ions ($P_{\mathrm{NBI},i} = P_{\mathrm{NBI},D} + P_{\mathrm{NBI},z}$) is a good approximation of χ_D.

The next step is the investigation of a case with $T_D > T_z$ in the pedestal top for discharge #38540, as shown in figure 6(b). Please note that the H correction has been applied to the T_D profile used in these simulations, as discussed in the appendix. Since there are no dedicated T_D measurements available in the plasma core in AUG, two assumptions have been made on the core T_D for two different simulations, which are shown in figure 12(a). The first input profile assumes that the offset between T_D and T_z in the pedestal top is maintained towards the plasma core (corresponding to Case 1, the solid red profile in figure 12(a)). For the second simulation, T_D converges to T_z in the plasma core (corresponding to Case 2, the dashed red profile in figure 12(a)). The two different input profiles constitute a sensitivity test of the results to the assumption on the shape of the core profiles.

Under both assumptions, the heat exchange term between main ions and impurities $P_{D,z}$ is non-zero (except for Case 2 in the core, as T_D collapses to T_z). For the main ion power balance, the heat exchange with impurities is a sink, as shown in figure 11(a). For the boron, $P_{D,z}$ is the dominant power input at the edge, and of a similar order of magnitude to the power input from NBI and ECRH in the core, as can be seen in figure 11(b). The energy source for the electrons is largely dominated by the ECRH power (note this is the highest input power case). The resulting heat fluxes are shown in figure 12(b). It can be seen that the assumption on the core profiles modestly affects Q, and consequently the χ calculation over the full radius. Maintaining the temperature difference between D and B at

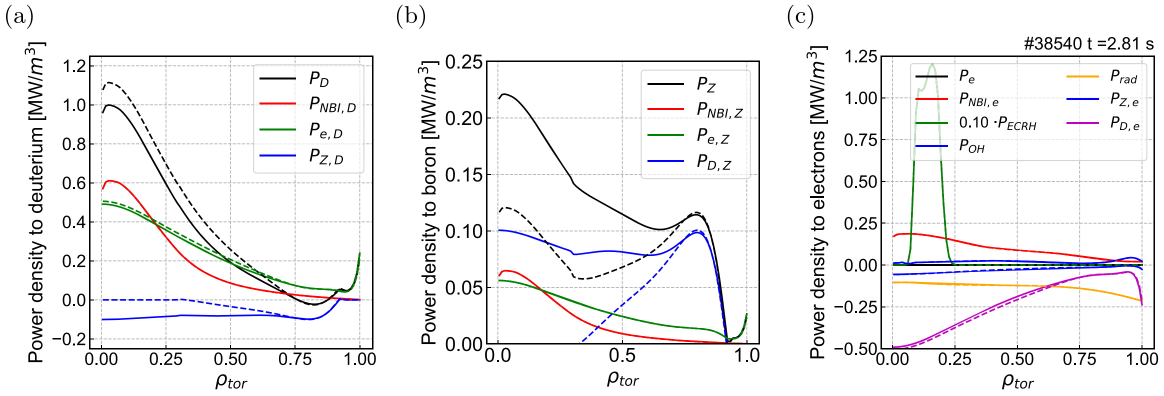

Figure 11. Power density profiles for (*a*) the main ions, (*b*) impurities and (*c*) electrons for discharge #38540. The individual contributions and sum, as stated in equations (3)–(5), are shown. The solid and dashed lines correspond to the input T_D profiles for Case 1 and Case 2 shown in figure 12(*a*).

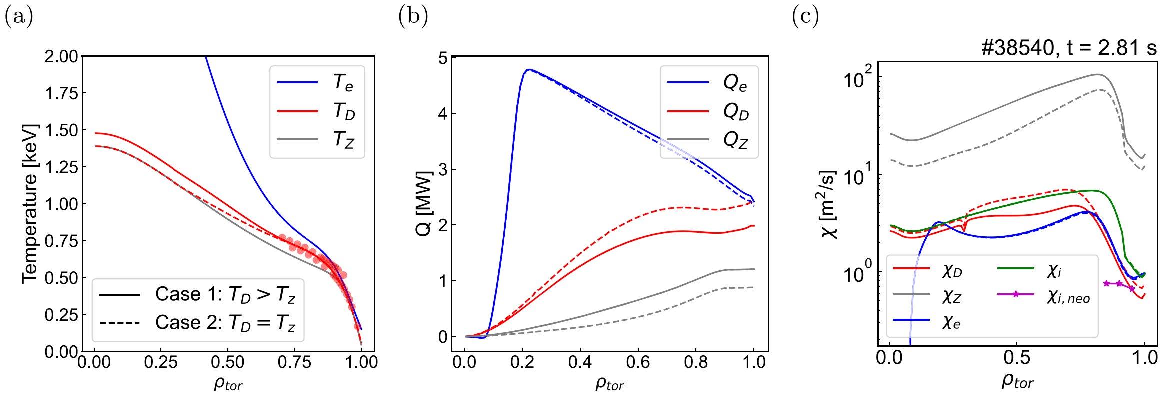

Figure 12. Main ion (red), impurity (gray) and electron (blue) (*a*) temperature profiles used as input for ASTRA simulations and (*b*) heat fluxes and (*c*) resulting heat diffusivities. The dashed lines correspond to the case with $T_D = T_z$ in the plasma core, while the solid line maintains the experimental temperature difference between the ion species at the pedestal top in the plasma core.

the plasma core, leads to a decrease of Q_D and an increase of Q_z, such that main ion and impurity heat fluxes are of a similar order of magnitude despite the impurities being only 2% of the total ion density. In fact, the impurity heat flux is higher than the main ion heat flux at the plasma edge. The resulting heat diffusivities are shown in figure 12(*c*). In this case, χ_z is around a factor of 10 higher than χ_D at midradius, and up to two orders of magnitude in the pedestal top. This is due to the fact that, while the impurity and main ion heat fluxes are of a similar order of magnitude, the main ion density is two orders of magnitude higher than the impurity density:

$$\begin{array}{l} \chi_z = -\dfrac{Q_z}{n_z \nabla T_z} \\ \chi_D = -\dfrac{Q_D}{n_D \nabla T_D} \end{array} \quad \rightarrow \quad \frac{\chi_z}{\chi_D} = \frac{Q_z}{Q_D}\frac{n_D}{n_z}\frac{\nabla T_D}{\nabla T_z}. \tag{7}$$

If we assume the temperature gradients are of a similar order of magnitude, $n_z = 0.01 \cdot n_D$, and since we have seen $Q_z \approx Q_D$ (figure 12(*c*)), then:

$$\frac{\chi_z}{\chi_D} = \frac{Q_z}{Q_D}\frac{n_D}{n_z}\frac{\nabla T_D}{\nabla T_z} \approx \frac{n_D}{n_z} \quad \rightarrow \quad \chi_z \approx 100 \cdot \chi_D. \tag{8}$$

In a simple picture, if the heat fluxes and temperature gradients are similar, n_z being two orders of magnitude smaller than n_D leads to χ_z being two orders of magnitude higher than χ_D. This means that when the energy source is similar on the main ions and impurities, the transport on the impurity channel must be much higher to sustain a similar temperature gradient and/or profile. As soon as there is a temperature difference between the main ions and the impurities, the heat exchange term becomes very large, and dominates the input power into the impurities, making the heat flux per particle for impurities much larger than for the main ions.

The assumption for the extrapolation of T_D towards the plasma core has a non-negigible impact on the results, leading to a factor of 3 variation of the χ_z and χ_D profiles, as can be seen by comparing solid and dashed profiles in figure 12. The impact of the H correction on the T_D profile on the χ_z/χ_D ratios is comparable, but lower, to that of the assumption made on the core T_D profile. The line integration correction on the T_z profile has a negligible impact on the χ_z/χ_D calculation, and therefore has not been applied to the input T_z profile. In this regard, the two core T_D profile cases illustrate the variability/uncertainty on the χ_z/χ_D from the experimental data. Note that in this case, χ_D is also close to the neoclassical value

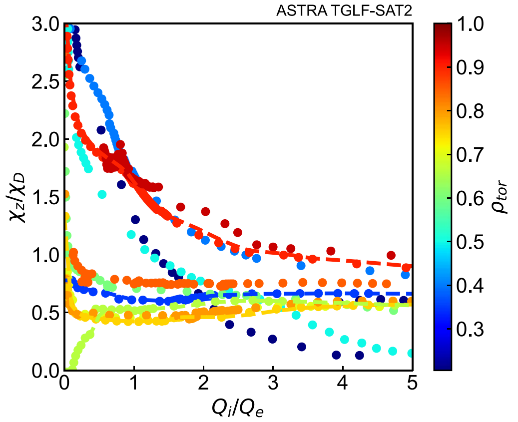

Figure 13. Impurity to main ion heat diffusivity ratio (χ_z/χ_D) as a function of the ion to electron heat flux (Q_i/Q_e) calculated with TGLF-SAT2, and used for ASTRA predictive simulations. The color code indicates the radial location, and example Legendre fits to the database are shown in dashed lines.

in the steep gradient region, and χ_i also provides a reasonable estimate of χ_D (which here uses $T_i = T_z$). For completeness, it has been checked that including additional impurity species in the analysis (in particular, carbon) does not have an impact on the analysis results.

4.2. Comparison to turbulence simulations

In this section, the comparison of experimental results (from power balance analysis) to turbulence transport models is presented. First, the gyro fluid TGLF-SAT2 code, one of the most widely used transport models [43–45], was used to derive a relation between the main ion and the impurity heat diffusivities as a function of the ion ($Q_i = Q_z + Q_D$) to electron heat flux (Q_i/Q_e) and the radial location, as shown in figure 13. The TGLF database has been built using experimental parameters and scanning RL_{T_D} to vary Q_i/Q_e. Please note that both experimental profiles from discharge #38539 and #38540 were used, which led to negligible variations in the database. The colour-code indicates the radial location, and it can be seen that the dependence of the χ_z/χ_D ratio varies at the distinct radial locations. The highest values are reached at the plasma edge ($\rho_{\mathrm{tor}} > 0.90$) and inside midradius ($\rho_{\mathrm{tor}} \approx 0.40$), where χ_z/χ_D increases as Q_i/Q_e decreases. At $\rho_{\mathrm{tor}} \approx [0.60, 0.80]$, χ_z/χ_D is reduced, and interestingly, shows the opposite dependence on Q_i/Q_e at $\rho_{\mathrm{tor}} \approx 0.66$. Overall, these χ_z/χ_D values, up to a factor of 3, are lower than those found from the power balance analysis, which showed minimum value of $\chi_z/\chi_D = Z$ for $T_D = T_z$. According to the power balance calculations, if the main ions are hotter than the impurities, χ_z/χ_D can reach even larger values. This would imply that, at high Q_i/Q_e, the impurities need to be hotter than the main ions, such that the $P_{D,z}$ is a sink in the impurity channel, and can result in $Q_z/n_z < Q_D/n_D$. Please note that the temperature difference $T_D - T_z$ does not need to be large to lead to a significant inter-ion species heat transfer $P_{D,z}$, as illustrated in figure 7. This would induce a large heat flux and a change in χ_z/χ_D.

In addition, the TGLF results have been compared to a database of linear gyrokinetic simulations [46, 47] (those simulations were part of a previous publication, and the reader is referred to [47] for further information). The simulations include trace B and C impurity ions and have been performed for the ion scales with the GKW code [48] at mid-radius ($\rho_{\mathrm{tor}} \approx 0.5$). The GKW results are shown in triangles in figure 14(*a*) (gray for Ion Temperature Gradient (ITG) modes, propagating in the ion drift direction, and black for Trapped Electron Modes (TEM), which propagate in the electron drift direction). The TGLF dataset shown in figure 13(*a*) is shown in blue stars for $\rho_{\mathrm{tor}} = 0.5$. The trend in the GKW and TGLF data is analogous: χ_z/χ_D ranges from values below 1 in strong ITG turbulence (large Q_i) to more than 10 (up to 35–40) for $Q_e > Q_i$ and corresponding linear mode frequencies approaching 0. In TEM, χ_z/χ_D also remains significantly larger than 1, usually with values between 5–10. The reason for the increase of the χ_z/χ_D ratio when decreasing Q_i/Q_e is related to a stronger resonant interaction of low positive (ion directed) frequency turbulence modes with impurities in comparison to main ions. This mechanism is well understood and has been studied analytically in detail in the context of impurity particle transport [46, 49]. The model predicts large variations of the χ_z/χ_D ratio, which peaks for positive mode frequencies approaching zero. The heat transport induced by ITG modes (of mode frequency ω_r) at a given k_y (binormal wavenumber) in the impurity channel can be larger than that of the main ion channel due to the 1/Z dependence of the drift frequency (ω_d). This is due to $(\omega_r - \omega_{d,z}) < (\omega_r - \omega_{d,D})$, where $\omega_{d,z}$ and $\omega_{d,D}$ are the drift frequencies of the impurity and main ions, respectively, such that for low ω_r ITG modes, impurity ion heat transport can be enhanced compared to main ion heat transport.

Please note that GKW considers the most unstable mode at each $k_y\rho_i$, neglecting additional transport by subdominant modes, while TGLF includes subdominant modes. Subdominant modes may be present that cause comparable transport in the main and impurity ion channel, which would lead to a reduction of the overall χ_z/χ_D ratio. This could explain the lower values retrieved from TGLF in comparison to GKW. Please note that a subset of non-linear GKW simuations are consistent with the quasi-linear results [50], which are shown in magenta pentagons in figure 14(*a*).

Figure 14(*a*) also shows the χ_z/χ_D values evaluated from power balance (red symbols) at mid-radius for discharge #38539 (squares) and #38540 (circles). It can be seen that data points obtained from the interpretation of the experimental data are qualitatively consistent with the trend of turbulence models: χ_z/χ_D increases as Q_i/Q_e decreases (in the experiment, when P_{ECRH} increases at constant P_{NBI}). At this location ($\rho_{\mathrm{tor}} = 0.5$), the values agree quantitatively.

In the context of this work, a database of 42 GKW linear runs at $\rho_{\mathrm{tor}} = 0.75$, extending the simulations towards the edge region, has been built. The results are shown in figure 14(*b*). The same trends are also visible at this outer radial location, although with more limited variation. Here, the interpretive results are larger than the turbulence models by more than an order of magnitude, and the GKW χ_z/χ_D values are larger than those from TGLF, as for $\rho_{\mathrm{tor}} = 0.50$.

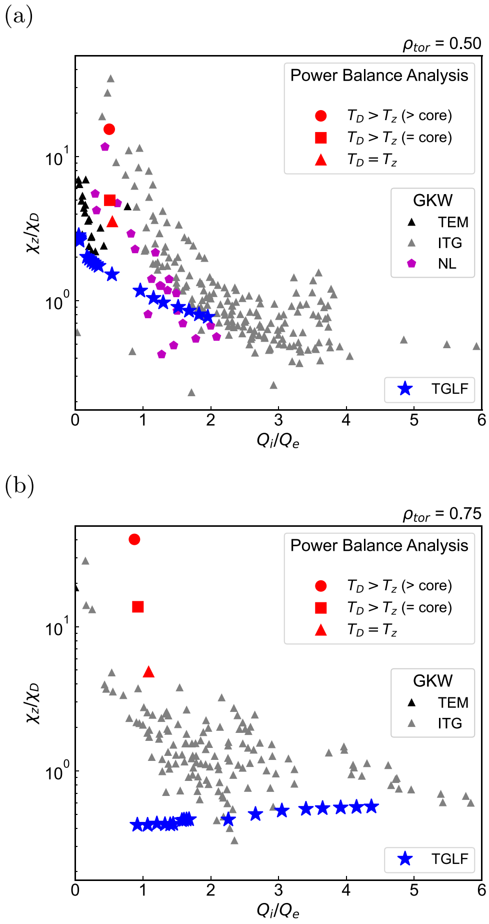

Figure 14. Impurity to main ion heat diffusivity as a function of the ion to the electron heat flux at (*a*) $\rho_{\text{tor}} = 0.5$ and (*b*) $\rho_{\text{tor}} = 0.75$. The stars show the results from TGLF-SAT2. The GKW results are shown in triangles, black for Trapped Electron Modes and gray for Ion Temperature Gradient modes. The results from the power balance analysis are shown in red symbols, a square and circle for Cases 1 and 2 corresponding to discharge #38540 ($T_D > T_z$) and a triangle for discharge #38539 ($T_D = T_z$), respectively. A subset of non-linear GKW simulations is shown in magenta pentagons in (*a*).

Dedicated GKW simulations for discharge #38540 have also been carried out, which are shown in figures 15(*a*)–(*c*). Figure 15(*b*) shows the χ_α spectra (where α refers to both the impurity and main ions, in solid and dashed lines, respectively) as a function of $k_y\rho_i$ for different radial locations. Please note that here ρ_i is the ion Larmor radius of the reference ion mass, in this case, deuterium. It can be see that the impurity χ peaks at higher $k_y\rho_i$ compared to deuterium, and that it exhibits a broader spectrum in $k_y\rho_i$. This is consistent with the fact that the boron Larmor radius is smaller than deuterium Larmor radius, such that the peak of impurity transport spectrum is shifted to higher $k_y\rho_i$ with respect to deuterium, which leads to a broader spectrum that can induce transport at lower wave numbers in comparison to the main ions. The χ_z/χ_D ratio as a function of the radial coordinate ρ_{tor} is shown in figure 15(*b*) for different $k_y\rho_i$ values. It can be seen that for all $k_y\rho_i$, the χ_z/χ_D ratio decreases from midradius towards the pedestal top, reaching minimum values at $\rho_{\text{tor}} \approx 0.75 - 0.80$. This result is consistent with the TGLF simulations, and this reduction of the χ_z/χ_D ratio is important to have a temperature separation between main ions and impurities, as will be discussed in the next subsection. An extended set of simulations with increased radial coverage, including the pedestal region, is shown in black stars (averaged over all $k_y\rho_i$). For all $k_y\rho_i$, χ_z/χ_D peaks at mid-radius and decays towards $\rho_{\text{tor}} \approx 0.75$ and, as shown in the black curve, increases back up in the pedestal top. This result is also consistent with the TGLF simulations, presented in figure 13. In addition, figure 15(*c*) shows χ_z/χ_D as a function of $k_y\rho_i$ at different radial locations, and it can be seen that at all radial locations the ratio increases with $k_y\rho_i$, which is consistent with figure 15(*a*). The compatibility of the properties of χ_z/χ_D discussed in this section, with T_z different from T_D has been tested with the ASTRA code and is presented in the following section.

4.3. Predictive heat transport analysis using turbulence models

In this section, the ASTRA code has been run in predictive mode to evaluate whether, and under which conditions, $T_D > T_z$ can be maintained, according to the results from turbulence simulations presented in the previous section. In the predictive approach, the heat fluxes (Q_α) are calculated from the energy sources and the heat conductivities (χ_α) are prescribed in space by a turbulence model. The heat transport equation (equation (1)) is then solved iteratively for T_α.

In this work, χ_D is evaluated from power balance and χ_z is calculated by using the χ_D from power balance and interpolating a 2D polynomial function of χ_D/χ_z for the Q_i/Q_e and ρ_{tor} values at each radial location. Here, T_z, is the free parameter, and the boundary condition $T_z = T_{z,\text{exp}}$ is imposed.

First, the TGLF dataset presented in figure 13 has been used. The dataset has been fitted to a 2D polynomial function (see dashed lines as reference). The fits are used for the estimation of χ_z at $\rho_{\text{tor}} > 0.2$, while for $\rho_{tor} < 0.2$ the core impurity heat transport is approximated by a simple formula based on gyro-Bohm scaling (at fixed B_{tor}) $\chi_z = 0.75 T_e^{3/2} q^2 R_0 / L_{T_i} (1 + 4\rho_{\text{tor}}^2)/7$, where q is the safety factor, R_0 the major radius and $L_{T_i} = |\partial T_i/\partial a|/T_i$.

The results for the time-dependent predictive simulations are shown in figures 16(*a*)–(*d*). Please note that the transparent profiles illustrate the evolution of (a) temperatures, (b) diffusivities, (c) heat fluxes and (d) heat flux and diffusivity ratios in each time step, while the solid profiles show the final converged values. The initial T_z profile is shown in green for reference in figure 16(*a*). In each time step, the difference between T_z and T_D is reduced, leading to reduced $P_{D,z}$, and consequently a decrease in Q_z (and χ_z) and an increase in Q_D (and χ_D). The drop of χ_z/χ_D at $\rho_{\text{tor}} \approx 0.75$ is essential to reproduce a temperature difference between T_D and T_z of 20 eV just inside the pedestal, of a lower value but in line with the experimental observation (50–60 eV). This

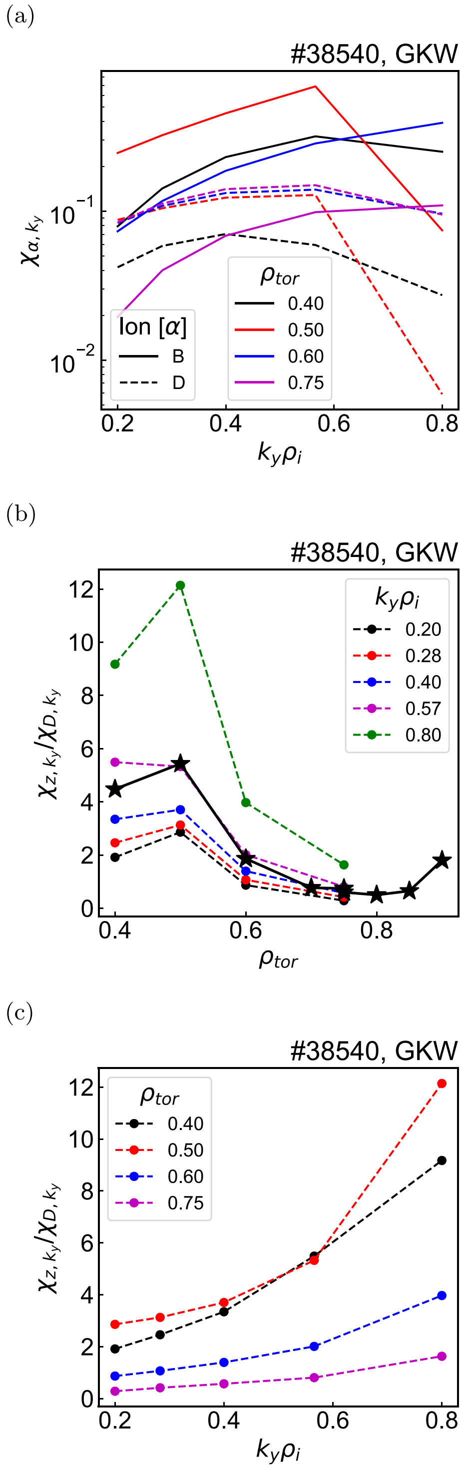

Figure 15. (*a*) Impurity (solid) and main ion (dashed) heat conductivity for each binormal wavenumber k_y, as a function of $k_y\rho_i$ at different radial locations. Here, $\chi_{\alpha,k}$ is computed as $\chi_{\alpha,k} \propto Q_{\alpha,k}/|\phi_k|^2/(R/L_T)$, where $Q_{\alpha,k}/|\phi_k|^2/(R/L_T)$ are the spectra of the quasi-linear weights of GKW runs. Impurity to main ion heat diffusivity as a function of (*b*) the radial coordinate ρ_{tor} for different $k_y\rho_i$ and (*c*) $k_y\rho_i$ for the different radial locations.

drop of the impurity heat diffusivity (improvement in heat confinement), leads to the build up of a temperature gradient, such that T_D and T_z equilibrate. The equilibration in turn leads to reduced heat exchange between the ion species, and a reduction of Q_z. Towards the core, T_z converges to (but is higher than) T_D, as shown in figure 16(*a*). This is due to the $\chi_z/\chi_D < Z$: in this case, a small temperature difference between impurities and D is sustained, as a large temperature difference would lead to too large power exchange between D and impurities, and χ_z/χ_D ratios that would not consistent with the used model. It has been verified that $T_D > T_z$ can be reproduced in the simulation when setting the T_D profile as initial T_z profile, and when changing the location of the boundary for T_z.

The temperature difference obtained using this model, which is on the order of 20 eV, is below the experimental temperature difference between T_D and T_z, which can be reduced to 50 eV taking into account all extended sources of uncertainty (discussed in the appendix). It was tested that, in order to recover a 50 eV temperature difference between main and impurity ions, the modeled χ_z/χ_D had to be increased a factor of 5. This is a reasonable increase of χ_z/χ_D, considering the results presented in the previous subsection: higher χ_z/χ_D values were recovered from the GKW simulations compared to the TGLF simulations. When artificially increasing these ratios, χ_z/χ_D ranges from 1.5 to 10, and a temperature difference of 50 eV can be recovered. However, as for the case in which the χ_z/χ_D ratios are taken from the TGLF dataset, the temperature difference profile peaks at 0.95, while the experimental T_D–T_z reaches its maximum at 0.85–0.90. Please note that when applying this model to discharge #38539 (see figure 6(*a*), with $T_D = T_z$), no temperature difference is recovered, in agreement with the experiment.

Lastly, a synthetic dataset of χ_z/χ_D values as a function of Q_i/Q_e and ρ_{tor} has been created. This toy model has been defined to find the values and the χ_z/χ_D dependence on ρ_{tor} that would be required to mantain a temperature difference resembling the experimental observation. The χ_z/χ_D profile is fixed at all radial locations, and shows an inverse dependence on Q_i/Q_e, decreasing from 7 to 1.5 (increases for $Q_i/Q_e < 2.5$ and stabilizes for $Q_i/Q_e > 5$). The profile is proportionally reduced to one third at $\rho_{\text{tor}} = 0.65$, then linearly reduced to 5% of its value at $\rho_{\text{tor}} = 0.70$ and increases back up to the $\rho_{\text{tor}} = 0.65$ profile at $\rho_{\text{tor}} = 0.75$. Using this toy model, where the χ_z/χ_D local minimum is at $\rho_{\text{tor}} = 0.70$, and the reduction is extended from $\rho_{\text{tor}} = 0.65 - 0.75$, a synthetic temperature difference that resembles the experimental one has been obtained. It gives a temperature difference of 60 eV at $\rho_{\text{tor}} = 0.88$ and decreases towards the steep gradient region. The resulting T_z profile and the temperature difference dT $= T_D - T_z$ for this simulation are shown in blue in figures 17(*a*) and (*b*), respectively. Please note that in this case a strong impurity temperature gradient is built at $\rho_{\text{tor}} = 0.85$, which leads to $T_z > T_D$ inside this location.

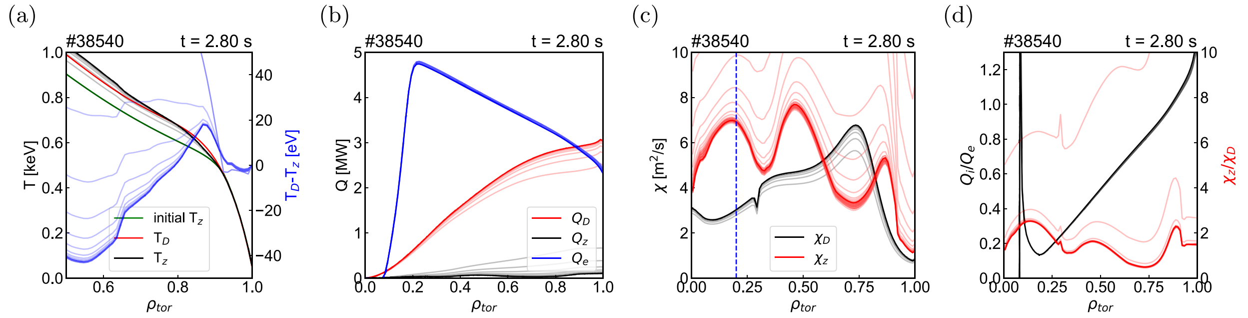

Figure 16. Main ion (red) and impurity (black) (*a*) temperature, (*b*) heat flux and (*c*) diffusivity profiles in time-dependent predictive ASTRA run for T_z, using the coefficients shown in figure 13. The converged profiles are shown in solid colors, while transparent profiles show each time step (*a*) Shows the initial (experimental) T_z profile in green and dT $= T_D - T_z$ in the right axis in blue. (*b*) Shows the electron heat flux in blue. (*d*) Q_i/Q_e (χ_z/χ_D) ratio in black (red) in the left (right) axis.

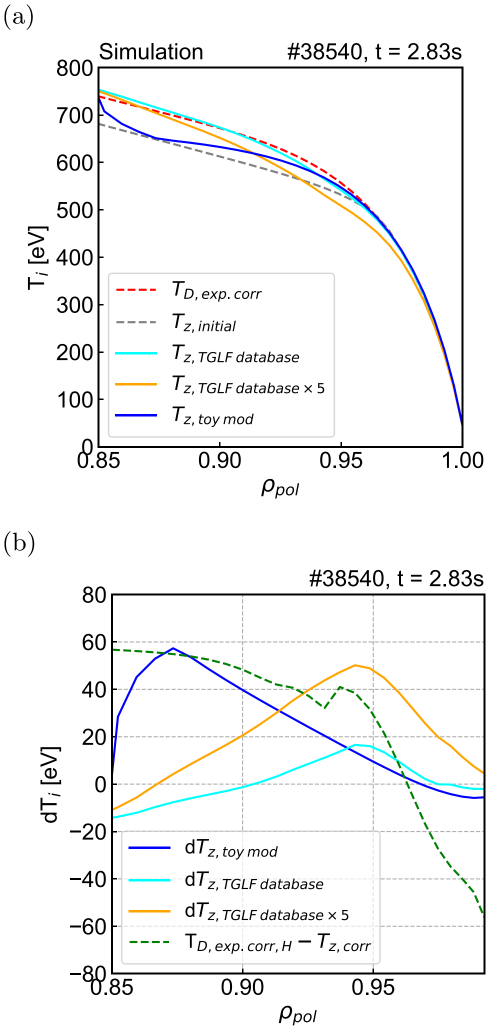

Figure 17. (*a*) Main ion experimental temperature profile (in dashed red), initial impurity temperature profile for simulations and predicted impurity profile using different χ_z/χ_D models discussed in this section. (*b*) Temperature difference between T_D and predicted T_z (solid lines) and the experimental temperature difference between main and impurity ions.

An overview of the simulation results, and a comparison to the experimental data, is presented in figures 17(*a*) and (*b*). Figure 17(*a*) shows the experimental main ion T profile and the impurity predicted profile using different models, while figure 17(*b*) presents the temperature differences d$T = T_D - T_z$, which correspond to figure 17(*a*). The main ion experimental profile, in dashed red, is an input to the simulations, and the initial T_z profile is shown in gray. The predictive profiles are shown in cyan and yellow, when using the dataset presented in figure 13 unmodified and multiplied by a factor of 5 (giving maximum χ_z/χ_D values in line with those obtained in the GKW simulations), respectively. The blue profile shows the results for the toy model described in the previous paragraph. It can be seen that $T_D > T_z$ can be recovered using these models. Figure 17(*b*) shows the temperature difference between the experimental T_D profile and the modeled T_z profiles (in solid lines) and the difference between the experimental T_D profile (including extended effects, discussed in the appendix) and the experimental T_z profile (including a line integration correction [51]) in dashed green. The difference recovered in the experiment, can be brought down to 50 eV, which is comparable to the temperature differences obtained with these models (from 20–50 eV), using χ_z/χ_D ratios and dependences with Q_i/Q_e and radius consistent with the TGLF and GKW simulations.

5. Experimental toroidal velocity measurements and comparison to neoclassical theory

In this section, the experimental deuterium toroidal velocity profiles for the discharges described in section 2 are presented. The difference between impurity and main ion toroidal velocity measurements serves as a test-bed for neoclassical theory, and their consistency can serve as a check for the validity of the MICX data analysis framework, and thus the temperature measurements.

While neoclassical transport theory provides a description for the ion poloidal flows [52, 53], the toroidal velocity, and consequently the radial electric field (E_r), are free parameters. The main ion poloidal velocity ($v_{\theta,D}$) depends on the temperature gradient only, while the impurity poloidal velocity ($v_{\theta,z}$) depends on both the main ion temperature and pressure gradients, and to a lesser extent, on the impurity pressure gradient. Since the radial force balance equation (which leads to an expression for the radial electric field, see equation (10)) is valid for any plasma species, the neoclassical difference

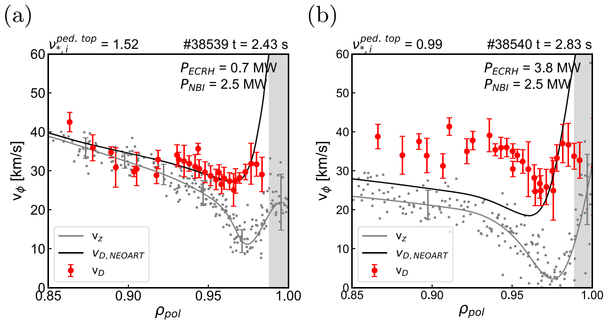

Figure 18. Experimental main ion (red) and impurity (gray) and neoclassically predicted main ion (black, from NEOART) toroidal velocity at (*a*) the *plateau* regime ($\nu_{*,i}^{\text{ped.top}} = 1.5$, $P_{\text{ECRH}} = 0.7$ MW) and (*b*) the banana limit ($\nu_{*,i}^{\text{ped.top}} \sim 1.0$, $P_{\text{ECRH}} = 3.8$ MW).

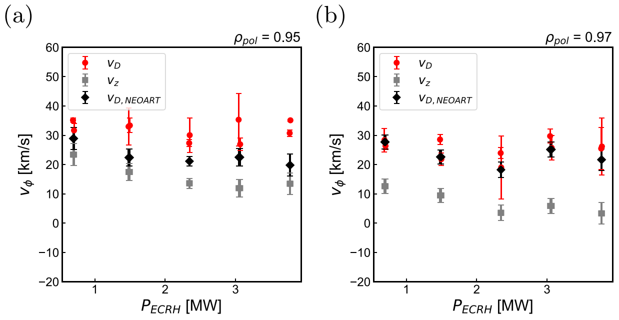

Figure 19. Main ion (red), impurity (gray) and neoclassical prediction (black) for the main ion toroidal velocity at (*a*) the pedestal top and (*b*) in the steep gradient region, as a function of ECRH input power for $P_{NBI} = 2.5$ MW.

($\Delta v_\phi^{\text{neo}}$) between the main ion ($v_{\phi,D}$) and the impurity ($v_{\phi,z}$) toroidal velocity can be calculated as:

$$\Delta v_\phi^{\text{neo}} = v_{\phi,D}^{\text{neo}} - v_{\phi,Z}^{\text{neo}} = \frac{v_{th,D} r_{L,D}}{2B_\theta} \frac{3}{2} K_2 \frac{1}{L_{T_i}}. \qquad (9)$$

where v_{th} is the thermal velocity, r_L is the Larmor radius, L_T is the temperature gradient scale length ($L_T^{-1} = \text{d}(\ln T)/\text{d}r$, r being the minor radius), L_p is the pressure gradient scale length and K_2 is collisionality-dependent viscosity coefficient [53]. This implies that the neoclassical calculation of $v_{\phi,D}$ is based on an input, i.e. the experimental $v_{\phi,z}$ or the experimental E_r profiles. The $v_{\phi,D,\text{NEOART}}$ profiles presented in this subsection rely on the experimental $v_{\phi,z}$ profile.

The neoclassical NEOART code has been used to calculate the neoclassical flows [41, 54], which are compared to experimental measurements. NEOART solves a system of linear coupled equations for the parallel velocities of multiple ion species, considering collisions of any species with the main ions and/or all other impurities, in all collision regimes, using a reduced charge state model.

The experimental main ion ($v_{\phi,D}$, in red) and impurity ($v_{\phi,z}$, in gray) toroidal velocity profiles are shown in figures 18(*a*) and (*b*) for discharges #38539 and #38540, respectively. The estimated neoclassical main ion toroidal velocity profile, calculated following the approach described above ($v_{\phi,D,\text{NEOART}} = v_{\phi,z} + \Delta v_\phi^{\text{NEOART}}$), is shown in black. Figure 18(*a*) refers to the consistency check case, firstly presented in figure 6(*a*). The experimental $v_{\phi,D}$ is consistent with neoclassical theory from $\rho_{\text{pol}} = 0.85$ to $\rho_{\text{pol}} = 0.98$, and features a rather flat shape and no pronounced dip in the steep gradient region. By applying the neoclassical correction to $v_{\phi,z}$, a good prediction of the minimum of $v_{\phi,D}$ is recovered, which is 20 km s^{-1} higher than $v_{\phi,z}$. This means that the difference between $v_{\phi,D}$ and $v_{\phi,z}$ is at the neoclassical level, and the dip feature of $v_{\phi,z}$ is due to the temperature gradient, following equation (9). Towards the separatrix, the ion pressure gradient length ($L_{p_i} = p_i/\nabla p_i$) becomes larger than the ion Larmour radius ($r_{L,i}$). The region where $L_{p_i} > r_{L,i}$ is indicated in gray (note that the radial coverage of this region varies from one case to another depending on the pressure gradient at the specific plasma conditions), where the local neoclassical description may not be sufficient. Note that the fact that thermal equilibration between ion species and good agreement of main ion toroidal velocity with neoclassical theory is found for #38539 $t = 2.43$ s serves as a valuable verification of the methodology used here and supports the reliability of the analysis.

In the highest P_{ECRH} case, figure 18(*b*), $v_{\phi,D}$ is in good agreement with $v_{\phi,D,\text{NEOART}}$ in the steep gradient region (at $\rho_{\text{pol}} = 0.97 - 0.98$). As the pedestal top is approached, $v_{\phi,D}$ increases and is faster than the neoclassical expectation (over 10 km/s at $\rho_{\text{pol}} = 0.95$). The strong gradient in $v_{\phi,D,\text{NEOART}}$ at $\rho_{\text{pol}} \sim 0.96$ coincides with the decoupling of T_D and T_z. If neoclassical transport was dominant in this region, a much more modest well feature would be expected in $v_{\phi,D}$. The difference between $v_{\phi,D,\text{NEOART}}$ and $v_{\phi,D}$ towards the pedestal top may be an indication of additional transport effects, such as turbulence, which in practice lead to a braking of $v_{\phi,z}$ (if $v_{\phi,z}$ were not available, and calculated from $v_{\phi,D}$ by applying a neoclassical correction, $v_{\phi,z,\text{NEOART}} > v_{\phi,z}$).

An overview of the impact of the input P_{ECRH} on $v_{\phi,D}$ and how it compares to impurities and neoclassical theory is shown in figures 19(*a*) and (*b*) at the pedestal top ($\rho_{\text{pol}} = 0.95$) and steep gradient region ($\rho_{\text{pol}} = 0.97$), respectively. The $v_{\phi,D}$ profiles are almost not affected by the input ECRH power, while $v_{\phi,z}$ decreases with P_{ECRH} at both locations. At the pedestal top, the neoclassical $v_{\phi,D}$ is in qualitative agreement with the experimental measurement, i.e. $v_{\phi,D}$ and $v_{\phi,D,\text{NEOART}}$ are higher than $v_{\phi,z}$. However, there are quantitative differences between $v_{\phi,D}$ and $v_{\phi,D,\text{NEOART}}$, such that neoclassical theory cannot fully describe the experimental measurement at the pedestal top in all conditions. This result is consistent with recent pedestal studies at AUG [55], which have shown that neoclassical transport is not sufficient to describe the full edge region in all AUG H-mode plasmas. In the steep gradient region, the neoclassical description is in remarkably good agreement with the experimental measurement, as can be seen in figure 19(*b*). This implies that the minimum of $v_{\phi,D}$ is correctly captured by neoclassical theory, i.e. ion transport in this region is close to the neoclassical level. This result is consistent with previous works at AUG [3, 18], which have shown evidence for the neoclassical nature of the ion flows in the

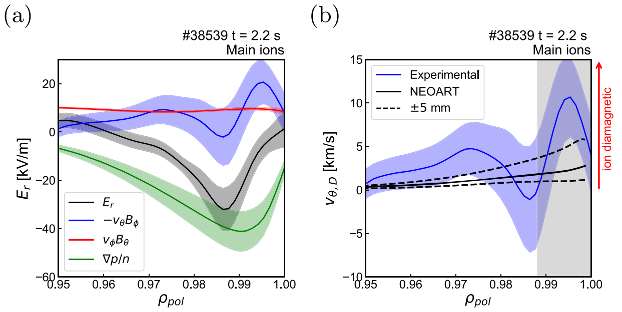

Figure 20. (a) Radial electric field profile (E_r) determined by impurity CXRS (black), experimental main ion pressure gradient term (green) and $v_\phi \cdot B_\theta$ (red) contributions to E_r and extracted main ion $v_\theta \cdot B_\phi$ (blue). (b) Experimentally determined main ion poloidal velocity ($v_{\theta,D}$, in blue) compared to neoclassical $v_{\theta,D}$ (in solid black). The uncertainty due to radial profile alignment is illustrated by the black dashed profiles.

steep gradient region using impurity measurements in H-mode plasmas. Please note these pedestals are still at relatively high collisionality (with maximum temperatures below 1 keV and density 4–5 $\cdot$ 10^{19} m^{-3}).

In addition to the direct measurement of T_D and $v_{\phi,D}$, the edge main ion diagnostic offers the ability to resolve $v_{\theta,D}$ experimentally. While the direct measurement of the edge $v_{\theta,D}$ is not available, this diagnostic enables its determination from measurements only, if an independent measurement of the radial electric field (E_r) is provided, via the radial force balance equation. In this way, the experimentally determined $v_{\theta,D}$ can be compared to the neoclassical description. The methodology is the following. First, the radial electric field (E_r) is evaluated using impurity CXRS measurements [56] and the magnetic field reconstruction, following the radial electric field equation [56, 57], which is valid for any plasma species α:

$$E_r = \frac{1}{n_\alpha q Z_\alpha}\frac{\partial p_\alpha}{\partial r} - v_{\theta,\alpha}B_\phi + v_{\phi,\alpha}B_\theta, \tag{10}$$

where B_ϕ and B_θ are the toroidal and poloidal magnetic field components, respectively. The experimentally determined E_r profile is shown in figure 20(a) in black. The $(1/n_D q_D)\cdot(\partial p_D/\partial r)$ and $v_{\phi,D}B_\theta$ contributions for the main ion radial force balance, shown in red and green in figure 20(a), are calculated using the experimental T_D and $v_{\phi,D}$ profiles, respectively. Note that here, $\partial n_D/(n_D \partial r) \approx \partial L_D/(L_D \partial r)$, where L_D is the D_α radiance. Since E_r is a property of the plasma, these three profiles can be combined to determine $v_{\theta,D}B_\phi$ (shown in blue in figure 20(a)), and from there, to extract $v_{\theta,D}$ from experimental measurements only (shown in blue in figure 20(b)). Note that for impurities, the dominant term in equation (10) is $v_{\theta,z}B_\phi$, while in the main ion radial force balance, the pressure gradient term is the dominant contribution [3, 56, 57]: the impurity diamagnetic term is small in comparison with the main ions, as it depends on Z_α^{-1}.

The experimentally derived main ion poloidal velocity profile is compared to the neoclassical main ion poloidal velocity calculated with the NEOART code in figure 20(b). The $v_{\theta,D}$ is small (<5 km s^{-1}) from the pedestal top to $\rho_{\mathrm{pol}} \sim 0.99$ and in the ion diagmagnetic drift direction. The dashed black profiles illustrate the sensitivity to a ±5 mm shift of the temperature profile (illustrative of the radial uncertainties of the measurements). Within this experimental uncertainty, $v_{\theta,D}$ is in good agreement in sign and magnitude with neoclassical theory, as shown by previous studies at AUG [3, 18, 56]. As the separatrix is approached, $v_{\theta,D}$ reaches values up to 10 km s^{-1}. Close to the separatrix, the direction of $v_{\theta,D}$ is consistent with the neoclassical expectation (positive, i.e. in the ion diamagnetic drift direction). However, the absolute magnitude is well above the neoclassical prediction. In this region (for $\rho_{pol} > 0.99$ indicated in gray, neoclassical ordering breaks down due to $r_{L,i} > L_{p_i}$), local calculations may not be appropriate and extended neoclassical effects may be necessary for a more accurate description of the measurement [58].

6. Conclusions and outlook

This work presents new insights in the field of ion heat transport and validation of neoclassical theory at the plasma edge of H-mode plasmas. A high resolution main ion charge exchange recombination spectroscopy system has been used to characterize, for the first time, deuterium temperature and toroidal velocity measurements at the plasma edge of a metal wall, which uses the same wall material foreseen for future fusion devices, such as ITER and DEMO. The diagnostic system, analysis tools and forward model used for the interpretation of the D_α spectra are described, alongside with dedicated experiments carried out at the ASDEX Upgrade tokamak to investigate the impact of collisionality and heating mix on T_D and $v_{\phi,D}$. The new temperature measurements have been interpreted with the ASTRA transport code, and compared to fluid (TGLF) and gyrokinetic (GKW) models. It has been found, both experimentally and in simulation, that the impurity to main ion conductivity (χ_z/χ_D) depends on the ion to electron heat flux (Q_i/Q_e). The difference between $v_{\phi,D}$ and $v_{\phi,z}$, in addition to experimentally determined $v_{\theta,D}$, have been compared to neoclassical codes (NEOART). The main results of the work are summarized here:

(i) The edge T_D and $v_{\phi,D}$ in H-mode plasmas have been documented for a variety of plasma heating schemes. These are state-of-the-art measurements in a full-tungsten device, presented in sections 3 and 5. The technique has been validated with a consistency check.

(ii) An unexpected difference between T_D and T_z ($T_D > T_z$) has been measured in certain plasma conditions. The discrepancy appears in cases with higher P_{ECRH} and/or Q_e. In view of this result, diagnostic effects that can affect the measurement were carefully examined, including halo, line integration effects, Stark, fine structure and Zeeman effects [16], the impact of having a H spectral contribution, passive background subtraction, impact of ELM dynamics, assumptions on the density profiles and uncertainty in the intensity calibration, fitting parameters and instrument response, which are discussed in detail in section 2 and the appendix.

(iii) Interpretive power balance analysis has shown us that:
  (a) χ_i can be used as a proxy of χ_D, but not for χ_z. This means that the characterization of the boron heat conductivity requires the multi-ion heat transport analysis presented here (splitting the ion heat transport equation in two separate equations for main ions and impurities, considering the heat transfer between them).
  (b) χ_z/χ_D depends on Q_i/Q_e. This has been observed experimentally, as shown in figures 14(*a*), (b) and is recovered in theoretical transport models, as discussed in the next points.
  (c) If $T_D = T_z$ (thus, $P_{D,z} = 0$), and there is no direct ion wave heating, $\chi_z = Z \cdot \chi_D$ (as heat exchange with electrons and NBI per particle scale with charge).
  (d) Thus, in the absence of direct wave ion heating (all heat is transferred via collisions) the fact that $\chi_z \neq Z \cdot \chi_D$ implies that temperature differences must exist. A small temperature difference between main and impurity ions, leads to high inter-ion species heat transfer and a large heat flux per particle in the impurity channel. Due to the large $P_{D,z}$ that is driven, if $Q_D \sim Q_z$, $\chi_z \approx 10 - 100\chi_D$, since $n_z \ll n_D$.

(iv) The χ_z/χ_D dependence on Q_i/Q_e is recovered by fluid (here, TGLF-SAT2) and gyrokinetic (GKW) transport models. In addition, the dependence has been reproduced by an analytical model [46] and it is understood to be due to ion resonance with turbulence modes. Both GKW and TGLF, reveal higher χ_z/χ_D ratios at mid-radius, which decay towards the pedestal top. The GKW χ_z/χ_D ratios can be an order of magnitude higher (20–30) than those recovered from TGLF (2–3), specially at low Q_i/Q_e. In the framework of this work, a new database of GKW simulations at $\rho_{tor} = 0.75$ has been built, as well as a database of TGLF simulations at for #38540 and #38539.

(v) Predictive transport analysis reveals that current fluid (here, TGLF-SAT2) and gyrokinetic (GKW) transport models can provide a plausible explanation for the temperature differences reported here experimentally. The TGLF and GKW χ_z/χ_D ratios are qualitatively consistent with those obtained from power balance analysis (see figures 14(*a*) and (*b*)), but are lower than them in the pedestal top. Using the TGLF χ_z/χ_D database for predictive modeling with ASTRA gives a 20 eV temperature difference between main and impurity ions, and a modest amplification of the χ_z/χ_D (in a factor of 5, consistent with the GKW results), reproduces a 50 eV temperature difference, which agrees with the experimental observation.

(vi) The decrease of χ_z/χ_D at $\rho_{\mathrm{tor}} = 0.75 - 0.80$, observed in the TGLF and GKW simulations, is essential to reproduce the temperature difference between T_D and T_z in predictive simulations.

(vii) Neoclassical theory provides a good description of $v_{\phi,D}$ in the steep gradient region ($\rho_{\mathrm{pol}} = 0.97$) in inter-ELM phases, but cannot describe $v_{\phi,D}$ towards the separatrix nor inside the pedestal ($\rho_{\mathrm{pol}} = 0.95$), depending on plasma collisionality. Closer to the highly collisional Pfirsch-Schlüter regime, the neoclassical description gives good results, but it fails in the banana regime. This is consistent with the edge/pedestal region being composed of different sub-regions, in which the dominant transport phenomena, and thus physics models needed to describe the data, change.

(viii) The deuterium poloidal velocity has been determined from measurements only, provided an independent measurement of E_r, and is found to be in good agreement with neoclassical theory in both magnitude and sign (in this case, ion diamagnetic drift direction) in the steep gradient region.

Importantly, result (iii-a) implies that using the T_z for the study of ion heat transport at the edge at the AUG tokamak is generally a valid assumption and has mild impact on the results. In comparison to DIII-D results, no negative ion heat fluxes are recovered when employing T_z for power balance analysis [15]. However, the diagnosis and use of main ion T_D profiles may be important for improving our understanding of ion heat transport and the validation of models. The temperature difference between T_D and T_z will be further investigated in the future with dedicated experimental and modeling efforts, with a special focus on the extension of the T_D measurements towards the plasma core and exploration of high Q_i/Q_e scenarios.

Acknowledgments

The first author wants to thank Dr G Tardini and Dr D Fajardo for their availability and support with ASTRA. This work has received funding from the EUROfusion Consortium (Grant Agreement No. CFP-TRED-AWP25-TRED-01) and the European Research Council (ERC) under the European Union's Horizon 2020 research and innovation programme (Grant Agreement No. 805162). This work has been partially carried out within the framework of the EUROfusion Consortium, funded by the European Union via the Euratom Research and Training Programme (Grant Agreement No. 101052200—EUROfusion). Views and opinions expressed are however those of the author(s) only and do not necessarily reflect those of the European Union or the European Commission. Neither the European Union nor the European Commission can be held responsible for them.

Appendix

The main ion deuterium measurements presented at AUG are routinely corrected for line integration and cross-section effects using the FIDASIM4 forward model (described in section 2.2), and fine structure, Zeeman effects and instrument function at spectral fitting (a more detailed discussion on the Zeeman, Stark, fine structure and gyromotion corrections can be found in [16]). In comparison, the boron impurity temperature measurements are routinely corrected at AUG for fine sctructure (FS) and Zeeman effects [56].

In this appendix, other possible sources of uncertainty in the interpretation of the main ion spectra beyond those described in section 2 and [16], that would lead to a correction of the real ion temperature profiles are discussed. These effects refer to the sensitivity of main ion spectral analysis to:

(i) *Hydrogen concentration.* The small energy difference for the electronic transition for H and D Balmer α line leads to superposed contributions to the spectra at 656.28 and 656.1 nm, respectively. A trace H concentration can potentially corrupt the interpretation of the D measurements, as it would lead to an apparent broadening of the spectral line which is not associated with T_D. The impact of having a H contribution has been evaluated using FIDASIM4. A H content of 15% leads to an overestimation of the D temperature up to 8% at the pedestal top (the correction decreases towards the separatrix), while a H concentration below 3%–6% can be safely assumed at AUG (which leads to a correction about 3%–4%).

(ii) *Absolute calibration and assumption on the deuterium density profile*: For an absolutely calibrated D_α spectra, and a precise comparison of experimental and synthetic spectra, the sensitivity of the optical system has to be accurately characterized. All CXRS systems at AUG are calibrated in-vessel and in the laboratory before and after the experimental campaign. The main ion system used in this work suffered a high heat flux event that deteriorated the transmission of the system, introducing an uncertainty in the spectral analysis. The impact of this event on the data interpretation has been minimized by a dedicated characterization of the degradation of the optical system by comparing the pre- and post- campaign calibration, and by tracking the signal level across regular standard H-mode discharges. Additionally, the brightness of the main ion spectra is directly related to the n_D profile. Given the uncertainty in the intensity calibration, large variations in the n_D profile would be consistent with the spectral brightness. Scaling the n_e and n_D profiles, while maintaining Z_{eff}, have been checked to have a negligible impact on the resulting temperature profile ($\text{d}T_D < 10$ eV, with no clear correlation between density and impact on temperature). Increasing the Z_{eff} value from 1 to 3 for discharge #38540, leads to a -40 eV offset of the T_D profile (note a large uncertainty $\Delta Z_{\text{eff}} = 1.0$ leads to a change of $\text{d}T$ of 20 eV, not sufficient to explain alone the temperature differences reported in this work). The reconstruction of n_D profiles using main ion CXRS is the subject of future work.

(iii) *Exclusion of spectral regions in the fit*: A geometrical filter has been installed in the MICX system to block the cold passive emission at 656.1 nm. The filter is necessary because this bright emission can potentially damage the instrumentation and distort the spectral measurement. The instrument response to the filter has been characterized through laboratory calibrations and is included in routine analysis. The spectral region affected by the filter is typically partially excluded for the fitting. The exclusion region has been determined from the laboratory calibration and by assessing the goodness of the fits, with the impact of the data exclusion on the fit output comprehensively characterized. This study has concluded that the optimal results are obtained for a exclusion region of $\lambda = [655.8, 656.4]$ nm. Symmetric and asymmetric changes in the exclusion region result in small changes in the temperature profiles ($\text{d}T < 20$ eV), but significantly affect the quality of the fits.

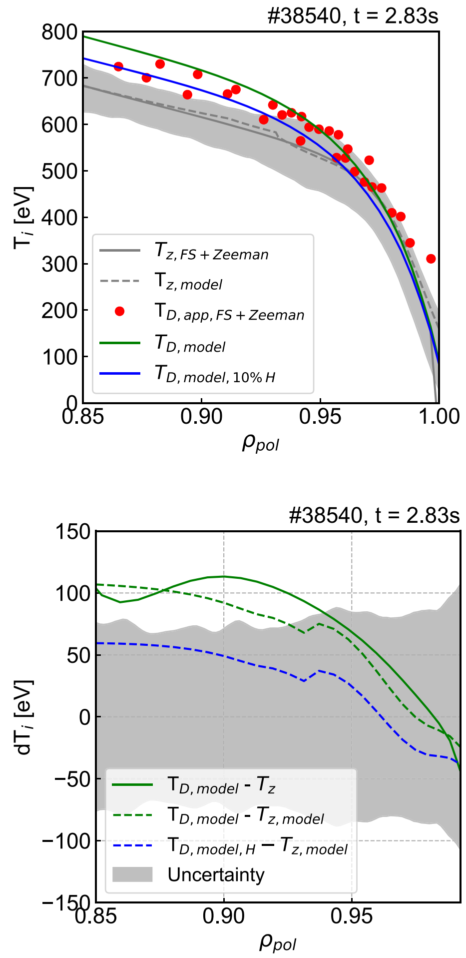

Figure A1. (*a*) Main ion (red, green and blue) and impurity (gray) temperature (T_α) profiles (*b*) and temperature difference ($\text{d}T = T_D - T_z$) between them accounting for different effects in the analysis for the high P_{ECRH} case presented in figure 6(*b*). $T_{D,\text{app,FS+Zeeman}}$ and $T_{z,\text{FS+Zeeman}}$ are obtained from direct fits to the experimental data, and corrected for fine structure and Zeeman effects. $T_{D,\text{model}}$ corrects for line integration, halo and cross-section effects using a forward model [16], while $T_{z,\text{model}}$ corrects for line integration effects [51]. $T_{D,\text{model},10\%\,H}$ accounts for a 10% concentration of hydrogen, which would affect the extracted temperature. As it can be seen in (*b*), accounting for all these effects, results in a temperature difference within the experimental uncertainty (the shadowed area in gray) in the experimental data and analysis process.

These effects are not routinely taken into account in the analysis of main ion spectra, and their joint effect on the comparison of T_D and T_z is examined for case #38540 presented in this paper. Their impact is illustrated in figure A1(*a*) and (*b*), which show the T_D and T_z profiles accounting for different effects in the data analysis and the temperature difference between them, respectively. Figure A1(*a*) shows the experimental impurity profile (which routinely includes the instrument function, FS and Zeeman corrections), and its errorbar in gray. The apparent main ion data is shown in red circles (this is the profile resulting from fitting the D_α spectra, including the instrument function, Zeeman and FS effects) and the true main ion temperature profile, after applying the forward model corrections, is shown in green. The discrepancy between the true T_D profile and the T_z profile (in gray) is higher than between the apparent T_D and T_z profiles in the pedestal top, as the forward model increases T_D profile, pushing it away from the T_z profile. In addition, a forward model has been recently developed that enables the correction of line integration effects on the evaluation of impurity profiles [51]. The corrected T_z profile is shown in dashed gray in figure A1(*a*). As for the main ions, the correction reveals a higher true T_z, and would bring the main ion and impurity temperature profiles to closer agreement. However, the correction is very subtle and within experimental uncertainty, and thereby not routinely included in impurity CXRS analysis, and also not considered in the ASTRA simulations carried out in this work. The impact of considering a maximum 6% H contribution to the main ion spectra is shown in blue, and leads to closer agreement between T_D and T_z profiles. The difference between the T_D and T_z profiles is illustrated in figure A1(*b*). The gray errorband includes experimental errorbars as well as the uncertainty due to effects *(i)* and *(iii)*. When considering the T_D and T_z profiles, including the line integration effects for the main ions only, or both for main ions and impurities (green solid and dashed lines, respectively), the difference between the two profiles is up to 100 eV in the pedestal top region, and decreases in the steep gradient region. When a contribution of H to the D spectra is considered, the temperature difference can be brought down to 50–60 eV in the pedestal top, shown in the blue dashed line. As can be seen, in this case, the temperature difference would fall within the experimental uncertainty of the measurement and data analysis methodology, illustrated by the gray errorband. Therefore, the difference between T_D and T_z inside the pedestal top presented for case #38540 could be explained by an accumulation of uncertainties that are not routinely taken into account. However, as discussed in section 3, the fact that this is not an isolated case and temperature differences may arise depending on experimental conditions gives confidence to the methodology employed for the interpretation of the data. This is further supported by the fact that cases where $T_D = T_z$ exist in the experiments analyzed within this work.

ORCID iDs

P. Cano-Megias 0000-0001-5182-6513
E. Viezzer 0000-0001-6419-6848
R.M. McDermott 0000-0002-8958-8714
C. Angioni 0000-0003-0270-9630
E. Fable 0000-0001-5019-9685
M. Cavedon 0000-0002-0013-9753
D.J. Cruz-Zabala 0000-0001-5925-5153

References

[1] Ryter F., Imbeaux F., Leuterer F., Fahrbach H.-U. and Suttrop W. (ASDEX Upgrade Team) 2001 Experimental characterization of the electron heat transport in low-density ASDEX Upgrade plasmas *Phys. Rev. Lett.* **86** 5498–501

[2] Mantica P. *et al* 2009 Experimental study of the ion critical-gradient length and stiffness level and the impact of rotation in the JET tokamak *Phys. Rev. Lett.* **102** 175002

[3] Viezzer E., Pütterich T., Angioni C., Bergmann A., Dux R., Fable E., McDermott R.M., Stroth U. and Wolfrum E. 2014 Evidence for the neoclassical nature of the radial electric field in the edge transport barrier of ASDEX Upgrade *Nucl. Fusion* **54** 012003

[4] Chankin A.V. *et al* 2006 SOLPS modelling of ASDEX Upgrade H-mode plasma *Plasma Phys. Control. Fusion* **48** 839–68

[5] Viezzer E. *et al* 2017 Investigation of inter-ELM ion heat transport in the H-mode pedestal of ASDEX Upgrade plasmas *Nucl. Fusion* **57** 022020

[6] Viezzer E. *et al* (The ASDEX Upgrade Team and The EUROfusion MST1 Team) 2018 Ion heat transport dynamics during edge localized mode cycles at ASDEX Upgrade *Nucl. Fusion* **58** 026031

[7] Pablant N.A. *et al* 2016 Investigation of ion and electron heat transport of high-T_e ECH heated discharges in the large helical device *Plasma Phys. Control. Fusion* **58** 045004

[8] Battaglia D.J., Burrell K.H., Chang C.S., deGrassie J.S., Grierson B.A., Groebner R.J. and Hager R. 2016 Improved kinetic neoclassical transport calculation for a low-collisionality QH-mode pedestal *Plasma Phys. Control. Fusion* **58** 085009

[9] Catto P.J., Parra F.I., Kagan G., Parker J.B., Pusztai I. and Landreman M. 2013 Kinetic effects on a tokamak pedestal ion flow, ion heat transport and bootstrap current *Plasma Phys. Control. Fusion* **55** 045009

[10] Stacey W.M. and Groebner R.J. 2007 Thermal transport analysis of the edge region in the low and high confinement stages of a DIII-D discharge *Phys. Plasmas* **14** 012501

[11] Gohil P., Burrell K.H. and Osborne T.H. 1998 Energy transport during off-axis neutral beam heating in the DIII-D tokamak *Nucl. Fusion* **38** 425–36

[12] Callen J.D., Groebner R.J., Osborne T.H., Canik J.M., Owen L.W., Pankin A.Y., Rafiq T., Rognlien T.D. and Stacey W.M. 2010 Analysis of pedestal plasma transport *Nucl. Fusion* **50** 064004

[13] Grierson B.A., Burrell K.H., Solomon W.M. and Pablant N.A. 2010 Deuterium velocity and temperature measurements on the DIII-D tokamak *Rev. Sci. Instrum.* **81** 10D735

[14] Haskey S.R., Grierson B.A., Stagner L., Burrell K.H., Chrystal C., Groebner R.J., Ashourvan A. and Pablant N.A. 2017 Deuterium charge exchange recombination spectroscopy from the top of the pedestal to the scrape off layer in H-mode plasmas *J. Instrum.* **12** C10013

[15] Haskey S.R. *et al* 2022 Ion thermal transport in the H-mode edge transport barrier on DIII-D *Phys. Plasmas* **29** 012506

[16] Cano-Megias P., Viezzer E., van Vuuren A.J., Cavedon M., Cruz-Zabala D.J., Dux R., Geiger B., Garcia-Munoz M. and Chacartegui R. 2019 Feasibility study for an edge main ion charge exchange recombination spectroscopy system at ASDEX Upgrade *J. Instrum.* **14** C10040

[17] Viezzer E., Pütterich T., Dux R. and McDermott R.M. 2012 High-resolution charge exchange measurements at ASDEX Upgrade *Rev. Sci. Instrum.* **83** 103501

[18] Cavedon M., Pütterich T., Viezzer E., Dux R., Geiger B., McDermott R.M., Meyer H. and Stroth U. 2017 A fast edge charge exchange recombination spectroscopy system at the ASDEX Upgrade tokamak *Rev. Sci. Instrum.* **88** 043103

[19] van Vuuren A.J., Geiger B., Jacobsen A.S., Cavedon M., Dux R. and Köhnlein H. 2019 An edge fast-ion D-alpha system installed at ASDEX Upgrade *Rev. Sci. Instrum.* **90** 103501

[20] Bell R.E. 2004 Exploiting a transmission grating spectrometer *Rev. Sci. Instrum.* **75** 4158

[21] Bolte N.G., Heidbrink W.W., Pace D., Van Zeeland M. and Chen X.I. 2016 Measurement and simulation of passive fast-ion D-alpha emission from the DIII-D tokamak *Nucl. Fusion* **56** 112023

[22] Scotti F., Stotler D.P., Bell R.E., LeBlanc B.P., Sabbagh S.A., Soukhanovskii V.A., Umansky M.V. and Zweben S.J. 2021 Outer midplane neutral density measurements and H-mode fueling studies in NSTX-U *Nucl. Fusion* **61** 036002

[23] Grierson B.A., Burrell K.H., Chrystal C., Groebner R.J., Kaplan D.H., Heidbrink W.W., Muñoz Burgos J.M., Pablant N.A., Solomon W.M. and Van Zeeland M.A. 2012 Active spectroscopic measurements of the bulk deuterium properties in the DIII-D tokamak *Rev. Sci. Instrum.* **83** 10D529

[24] Grierson B.A., Burrell K.H., Heidbrink W.W., Lanctot M.J., Pablant N.A. and Solomon W.M. 2012 Measurements of the deuterium ion toroidal rotation in the DIII-D tokamak and comparison to neoclassical theory *Phys. Plasmas* **19** 056107

[25] Grierson B.A., Burrell K.H., Chrystal C., Groebner R.J., Haskey S.R. and Kaplan D.H. 2016 High resolution main-ion charge exchange spectroscopy in the DIII-D H-mode pedestal *Rev. Sci. Instrum.* **87** 11E545

[26] Haskey S.R., Grierson B.A., Burrell K.H., Chrystal C., Groebner R.J., Kaplan D.H., Pablant N.A. and Stagner L. 2016 Measurement of deuterium density profiles in the H-mode steep gradient region using charge exchange recombination spectroscopy on DIII-D *Rev. Sci. Instrum.* **87** 11E553

[27] Haskey S.R. *et al* 2018 Active spectroscopy measurements of the deuterium temperature, rotation and density from the core to scrape off layer on the DIII-D tokamak *Rev. Sci. Instrum.* **89** 10–110

[28] Geiger B. *et al* 2020 Progress in modelling fast-ion D-alpha spectra and neutral particle analyzer fluxes using FIDASIM *Plasma Phys. Control. Fusion* **62** 105008

[29] Stagner L., Geiger B., and Heidbrink W.W. 2020 FIDASIM: a neutral beam and fast-ion diagnostic modeling suite *Zenodo* https://doi.org/10.5281/zenodo.1341369 Repository published on 5th August 2020

[30] van Vuuren A.J., Geiger B., Schneider P.A., Bogar K., Poloskei P.Z., Cathey A., Hoelzl M., Jacobsen A.S., Cavedon M. and Dux R. (the ASDEX Upgrade Team) 2021 Experimental study of ELM induced fast-ion transport using passive FIDA spectroscopy at the ASDEX Upgrade tokamak *Nucl. Fusion* **61** 046001

[31] Cano-Megias P. 2022 Characterization of main ion properties for the optimization of future fusion power plants *PhD Thesis* Universidad de Sevilla (Sevilla) (available at: https://hdl.handle.net/11441/142823)

[32] Weiland M., Geiger B., Jacobsen A.S., Reich M., Salewski M. and Odstrcil T. 2016 Enhancement of the FIDA diagnostic at ASDEX Upgrade for velocity space tomography *Plasma Phys. Control. Fusion* **58** 025012

[33] Hirvijoki E., Asunta O., Koskela T., Kurki-Suonio T., Miettunen J., Sipilä S., Snicker A. and Äkäslompolo S. 2014 ASCOT: solving the kinetic equation of minority particle species in tokamak plasmas *Comput. Phys. Commun.* **185** 1310–21

[34] Stix T.H. 1972 Heating of toroidal plasmas by neutral injection *Plasma Phys.* **14** 367–84

[35] Wesson J. 2011 *Tokamaks* 4th edn (Oxford University Press)

[36] Weisen H., Delabie E., Flanagan J., Giroud C., Maslov M., Menmuir S., Patel A., Scott S., Siren P. and Varje J. 2020 Analysis of the inter-species power balance in JET plasmas *Nucl. Fusion* **60** 036004

[37] Pereverzev G.V. and Yushmanov P.N. 2002 Automated system for transport analysis *Technical Report* (Max-Planck-Institut für Plasmaphysik)

[38] Fable E. *et al* 2013 Novel free-boundary equilibrium and transport solver with theory-based models and its validation against ASDEX Upgrade current ramp scenarios *Plasma Phys. Control. Fusion* **55** 124028

[39] Zhdanov V.M. 2002 *Transport Processes in Multicomponent Plasma* (CRC Press)

[40] Huba J.D. 1998 NRL plasma formulary *Includes Bibliographical References* (Naval Research Laboratory) Revised 1998 pp 61–64

[41] Peeters A.G. 2000 Reduced charge state equations that describe Pfirsch Schlüter impurity transport in tokamak plasma *Phys. Plasmas* **7** 268–75

[42] Galeev A.A. and Sagdeev R.Z. 1968 Transport phenomena in a collisionless plasma in a toroidal magnetic system *Sov. Phys. - JETP* **26** 233–40

[43] Staebler G.M., Belli E.A., Candy J., Kinsey J.E., Dudding H. and Patel B. 2021 Verification of a quasi-linear model for gyrokinetic turbulent transport *Nucl. Fusion* **61** 116007

[44] Staebler G.M., Candy J., Belli E.A., Kinsey J.E., Bonanomi N. and Patel B. 2021 Geometry dependence of the fluctuation intensity in gyrokinetic turbulence *Plasma Phys. Control. Fusion* **63** 015013

[45] Staebler G., Bourdelle C., Citrin J. and Waltz R. 2024 Quasilinear theory and modelling of gyrokinetic turbulent transport in tokamaks *Nucl. Fusion* **64** 103001

[46] Angioni C. 2015 Gyrokinetic study of the impact of the electron to ion heating ratio on the turbulent diffusion of highly charged impurities *Phys. Plasmas* **22** 102501

[47] McDermott R.M., Angioni C., Cavedon M., Kappatou A., Dux R., Fischer R. and Manas P. (the ASDEX Upgrade Team) 2022 Validation of low-Z impurity transport theory using boron perturbation experiments at ASDEX Upgrade *Nucl. Fusion* **62** 026006

[48] Peeters A.G., Camenen Y., Casson F.J., Hornsby W.A., Snodin A.P., Strintzi D. and Szepesi G. 2009 The nonlinear gyro-kinetic flux tube code GKW *Comput. Phys. Commun.* **180** 2650–72

[49] Angioni C. 2021 Impurity transport in tokamak plasmas, theory, modelling and comparison with experiments *Plasma Phys. Control. Fusion* **63** 073001

[50] Manas P. 2024 private communication

[51] Takacs R.. 2024 Development and application of a forward model for CXRS measurements on the ASDEX Upgrade tokamak *Master's Thesis* Technical University of Munich

[52] Hirshman S.P. and Sigmar D.J. 1977 Neoclassical transport of a multispecies toroidal plasma in various collisionality regimes *Phys. Fluids* **20** 418–26

[53] Kim Y.B., Diamond P.H. and Groebner R.J. 1991 Neoclassical poloidal and toroidal rotation in tokamaks *Phys. Fluids B* **3** 2050–60

[54] Dux R. and Peeters A.G. 2000 Neoclassical impurity transport in the core of an ignited tokamak plasma *Nucl. Fusion* **40** 1721–9

[55] Luda T. *et al* (the ASDEX Upgrade Team and the EUROfusion MST1 Team) 2021 Validation of a full-plasma integrated modeling approach on ASDEX Upgrade *Nucl. Fusion* **61** 126048

[56] Viezzer E. *et al* 2013 High-accuracy characterization of the edge radial electric field at ASDEX Upgrade *Nucl. Fusion* **53** 053005

[57] McDermott R.M. *et al* 2009 Edge radial electric field structure and its connections to H-mode confinement in Alcator C-Mod plasmas *Phys. Plasmas* **16** 056103

[58] Hinton F.L., Kim J., Kim Y.-B., Brizard A. and Burrell K.H. 1994 Poloidal rotation near the edge of a tokamak plasma in H-mode *Phys. Rev. Lett.* **72** 1216–9